

# Guiding Self-Organization in Active Matter with Spatiotemporal Boundary Conditions

Thesis by  
Tyler David Ross

In Partial Fulfillment of the Requirements for the  
Degree of  
Doctor of Philosophy

The logo for the California Institute of Technology (Caltech), featuring the word "Caltech" in a bold, orange, sans-serif font.

CALIFORNIA INSTITUTE OF TECHNOLOGY  
Pasadena, California

2020  
Defended March 27th, 2020

© 2020

Tyler David Ross  
ORCID: 0000-0002-7872-3992

All rights reserved.

## ACKNOWLEDGEMENTS

Life is too short to do boring science. Without a doubt, Matt Thomson has provided me with the rare opportunity to pursue unconventional research. He taught me not to be afraid of my own ideas and embrace my creativity. I am forever in debt to him for his tremendous support and mentorship.

Caltech will always be one of my favorite places. The ability to easily interact with people across departments has broadened my scientific horizons more than I could have imagined. I sincerely believe that this work would not exist without the fantastic support from the Caltech community.

I would like to thank:

Heun Jin Lee - without his optics prowess, scientific insights, three-by-three grids, Broad cafe kale salads, and late night discussions, this work would not have been possible.

Rachel Banks - whose exquisite writing skills, thoughtful scientific discussions, artisanal quality baking, and overall inspiring character made writing the paper a brilliant process.

Rob Phillips - for providing inspiration and the amazing people and resources that made it possible to do this research.

Zvonimir Dogic and Linnea Metcalf - for sharing their knowledge about the behaviors of the kinesin-microtubule system. In particular, their surface passivation technique was incredibly valuable for getting the system reliably working.

Emeric Charles - for holding my hand as I first dipped my toes into protein purification.

Manu Prakash - for encouraging me to do research that inspired me, even if it was well outside of my existing skill set. "If you were already an expert, then you wouldn't need to do a PhD."

Koen van den Dries - for sprinkling some of his imageJ wizardry on my microscopy images.

Yuri Lazebnik - whose wonderful stories always managed to carry me through dark times.

Martin Schwartz - for giving me the best advice right before the start of my PhD, namely, not to take anyone's advice.

Morton Silverberg, my grandfather - for being such an inspiring figure and always asking deep and thoughtful questions.

Phillis Silverberg, my grandmother - for being so supportive and tolerating the long technobabble discussions I've held with my grandfather.

Dan Ross, my father - for helping foster my love of science.

Judy Ross, my mother - for always being a reliable source of support.

Ben Ross, my brother - for sharing his wisdom from his PhD experience and for not hitting me too hard on the head as a child so that I could still manage to do half-decent science in my adult years.

## ABSTRACT

In this thesis, I demonstrate that self-organized structures and forces can be guided by modulating the interactions between force-generating molecules in space and time. The physics of self-organizing systems is an open frontier. We do not have a complete set of principles that can describe how a dynamic structure forms based on the non-equilibrium dynamics of its constituent components. Yet, living systems appear to depend on some set of rules of self-organization in order to reliably carry out their mechanical functions. Force-generating, active molecules in the form of motor proteins and filamentous polymers are responsible for performing fundamental tasks in living matter, such as locomotion and division. While it is known that the regulation of motor-filament interactions is necessary to achieve the dynamic structures that drive movement and propagation, the role of spatial and temporal patterning in self-organizing systems has not been explored. I design an artificial system of purified molecules where the interactions between motors and filaments are toggled with light. By patterning molecular interactions in space and time, I show that it is possible to localize the formation of spherically symmetric asters, which can be moved, merged, and used to generate advective fluid flows. The ability to pattern molecular interactions in space and time offers a new perspective in the search for principles of active self-organization. Spatial and temporal control makes it possible to start distilling how the interactions between active molecules determine the mesoscopic behaviors of self-organized structures. These rules ultimately govern the physics of living matter and may eventually be harnessed to build new materials and cell-like machines.

## PUBLISHED CONTENT AND CONTRIBUTIONS

1. Ross, T. D., Lee, H. J., Qu, Z., Banks, R. A., Phillips, R. & Thomson, M. Controlling organization and forces in active matter through optically defined boundaries. *Nature* **572**, 224–229. ISSN: 1476-4687. doi:10.1038/s41586-019-1447-1 (2019).

T.D. Ross is the primary and co-corresponding author, performed all experiments other than the gliding assay, and conducted all analyses except the fluid flow.

## TABLE OF CONTENTS

Acknowledgements . . . . .	iii
Abstract . . . . .	v
Published Content and Contributions . . . . .	vi
Table of Contents . . . . .	vi
List of Illustrations . . . . .	viii
Chapter I: Introduction . . . . .	1
1.1 Self-Organizing Active Matter . . . . .	1
1.2 Review of Motor-Filament Systems . . . . .	3
Chapter II: Controlling Organization and Forces in Active Matter Through Optically-Defined Boundaries . . . . .	21
2.1 Introduction . . . . .	21
2.2 Optical Control Over Aster Formation . . . . .	21
2.3 Aster Dynamics . . . . .	36
2.4 Programming Aster Patterning and Trajectories with Light . . . . .	42
2.5 Controlling Advective Fluid Flow With Active Matter . . . . .	43
2.6 Conclusion . . . . .	58
2.7 Methods and Materials . . . . .	58
Chapter III: Discussion of the Speed Amplification Effect . . . . .	68
Chapter IV: Conclusion . . . . .	73

## LIST OF ILLUSTRATIONS

<i>Number</i>	<i>Page</i>
1.1 An overview of artificial leashed and unleashed motor-filament systems	4
1.2 Schematic of motor binding dynamics . . . . .	14
2.1 Light-switchable active matter system enables optical control over aster formation, decay, and size. . . . .	22
2.2 3D projections of asters from z-stacks imaged with a 20x objective. .	24
2.3 Analysis of microtubule distribution in 3D. . . . .	25
2.4 Time series of light induced aster formation, decay, then formation. .	29
2.5 A comparison of model fittings for a contracting aster experiment. . .	30
2.6 Characteristic times for contraction and merger as functions of acti- vation length scales. . . . .	30
2.7 Plot of mean variance of image intensity as a function of time for different initial aster sizes. . . . .	33
2.8 Measuring the conservation of labeled fluorescent microtubules in the excitation region during aster formation. . . . .	35
2.9 Moving and merging operations of asters with dynamic light patterns.	37
2.10 The speed at which an aster returns to the center of the light pattern once the pattern stops moving. . . . .	38
2.11 Aster following a 50 $\mu\text{m}$ disk moving at 200 nm/s from right to left. .	40
2.12 Intensity of an aster for a light pattern moving at 200 nm/s. . . . .	41
2.13 Velocity distribution of gliding microtubules. . . . .	42
2.14 Operations for creating and moving asters are composed to make different desired patterns and trajectories. . . . .	43
2.15 Advective fluid flow is created and controlled with patterned light. . .	44
2.16 Minimum length experiment for a $L \times 20 \mu\text{m}$ excitation pattern. . . .	46
2.17 Minimum height experiment for a $350 \times H \mu\text{m}$ excitation pattern. . .	47
2.18 Minimum angle experiment for two $350 \times 20 \mu\text{m}$ excitation patterns. .	48
2.19 Minimum aster size experiment for disk patterns. . . . .	49
2.20 Flow velocity field generated with a 350 $\mu\text{m}$ activation bar measured with PTV of tracer particles. . . . .	50
2.21 A flow field measured at three different z-positions separated by 20 $\mu\text{m}$ .	51
2.22 Velocity field averaged over 7.5-minute intervals in a single experiment.	52

2.23	The average maximum speed for four different 7.5-minute time windows. . . . .	52
2.24	The correlation coefficient as a function of distance. . . . .	53
2.25	Flow field generated by 14 Stokeslets to model the 350 $\mu\text{m}$ activation bar case. . . . .	55
2.26	Demonstration of the linearity of the flow field. . . . .	56
2.27	Theoretical simulation of fluid flows under complex light patterns using Stokeslets. . . . .	57
2.28	Kinesin motor coding regions. . . . .	59
2.29	Length distribution of microtubules. . . . .	61
3.1	An illustration depicting a potential mechanism of the speed amplification effect in 1D. . . . .	69

*Chapter 1*

## INTRODUCTION

**1.1 Self-Organizing Active Matter**

The principles through which force-generating particles can come together and organize into dynamic structures is beyond the full grasp of our current technologies and theories. In nature, the complex phenomena that can be achieved by self-organizing systems is most prominent in living matter. The basic unit of life, the cell, remains unique in its ability to navigate through micron-scale environments, organize molecular cargo, and self-replicate. What are the governing rules of self-organization that make it possible for a cell to integrate chemical [1], electromagnetic [2], and mechanical [3] information from its environment and perform mechanical tasks accordingly? How can we construct systems that exhibit the same properties?

The non-equilibrium phenomenon of self-organization is performed in living matter by a collection of active molecules. Here, an active molecule is defined as a particle that repeatedly converts free energy into mechanical work. While the theories of equilibrium statistical mechanics have been immensely successful in predicting the behavior of a wide variety of systems, ranging from quantum to astrophysical, they cannot completely describe active matter systems. Equilibrium theories depend on detailed balance, where the transition rates between any two microstates is pairwise balanced. However, detailed balance is violated in active matter [4–6]. Although self-assembly can be described through the minimization of free energy, the process of self-organization follows a different set of principles.

Active self-organization is also distinct from passive self-assembly in terms of computational complexity. The most efficient self-assembly systems are able to form structures in linear time [7]. However, active self-organizing systems, where molecules can push and pull on each other, are uniquely capable of exponential growth and parallelized synchronization between molecules [8, 9]. These properties allow active systems to rapidly form dynamic structures that exert mesoscopic forces, such as flagella or muscle fibers.

The active molecules in the cell consist of polymerizing filaments and motors that translate across filaments. The motor-filament system is presently the only active matter system that self-organizes across nanometer to millimeter length scales.

An archetypal example of a self-organized motor-filament structure is the mitotic spindle, which pulls unique copies of each chromosome to opposite poles of the cell during division. Although the organization of the spindle involves many scaffolding and signaling proteins [10], artificial systems of purified motors and filaments have been built that are also capable of self-organization.

Artificial motor-filament systems, which I will review in the next section, have been shown to be capable of generating flows and organizing them into structures such as spools and asters. However, the generation of these forces and structures occur spontaneously and throughout the entire system. In contrast, living matter is able to precisely guide when and where self-organized forces and structures form. We currently lack principles for guiding self-organization, which are responsible for the ability of living materials to perform mechanical tasks. To begin identifying principles of guided self-organization, we need an experimental system where we can determine when and where active molecules interact.

Significant progress has been made in controlling the *structures* formed by complex molecular systems. Recent advancements in DNA nanotechnology have made it feasible to craft intricate architectures with thousands of nanometer-scale features. For example, techniques like DNA origami [11] have been utilized to organize tile arrays in arbitrary patterns [12] and allowed for the precise arrangement of emitters in photonic crystals [13]. However, the structures that have so far been achieved are nearly static in comparison to the dynamic cytoskeletal networks observed in living matter. The typical DNA motor moves 50,000 times slower than protein motors, where even the fastest DNA motor [14] can travel little more than a micrometer over the course of an hour. Thus a major challenge in advancing the field of nanotechnology is to incorporate *fast dynamics* such that structures can be formed or reconfigured on the timescale of seconds to minutes on a *mesoscopic* length scale. While my thesis emphasizes principles of self-organization, it can also be viewed as an advance in nanotechnology, where nanometer-scale interactions between molecular motors are controlled to organize dynamic structures that rearrange quickly at the micrometer length scale.

The focus of this thesis is on the localization of self-organization in artificial motor-filament systems. This first chapter is a review of self-organizing motor-filament systems. The second chapter is my work on guiding self-organization in a motor-filament system through spatiotemporal boundary conditions. Finally, the third chapter is an outlook of future directions in the field of active self-organization.

## 1.2 Review of Motor-Filament Systems

Here I will briefly review artificial systems of purified motor-filament biomolecules and the principles of self-organization they reveal. For clarity, I divide these experimental systems into two categories: (1) leashed, where motors are bound to a surface (or commonly known as a gliding assay), and (2) unleashed, where motors are free-floating. These systems consist of three main components: filamentous polymers, molecular motors, and a chemical fuel for the motors. More specifically, they use stabilized microtubule filaments, kinesin-1 motors, and ATP. Microtubules have a polarity in their structure, allowing for the designation of a plus and minus end. Kinesin-1 motors bind to microtubules and walk towards the plus end through ATP hydrolysis. It is worth noting that the microtubules in these experiments are stabilized, meaning they are not undergoing polymerization or depolymerization as they do inside of cells. This review will not include actomyosin systems because they lack an extensive body of work compared to kinesin-microtubule systems. I am also not discussing other microtubule motor proteins, such as dynein, because their properties have largely not been explored in the context of artificial self-organizing systems. For a discussion of some of the experimental details see Section 1.2.2. I also briefly review efforts to model the motor-filament system in Section 1.2.3.

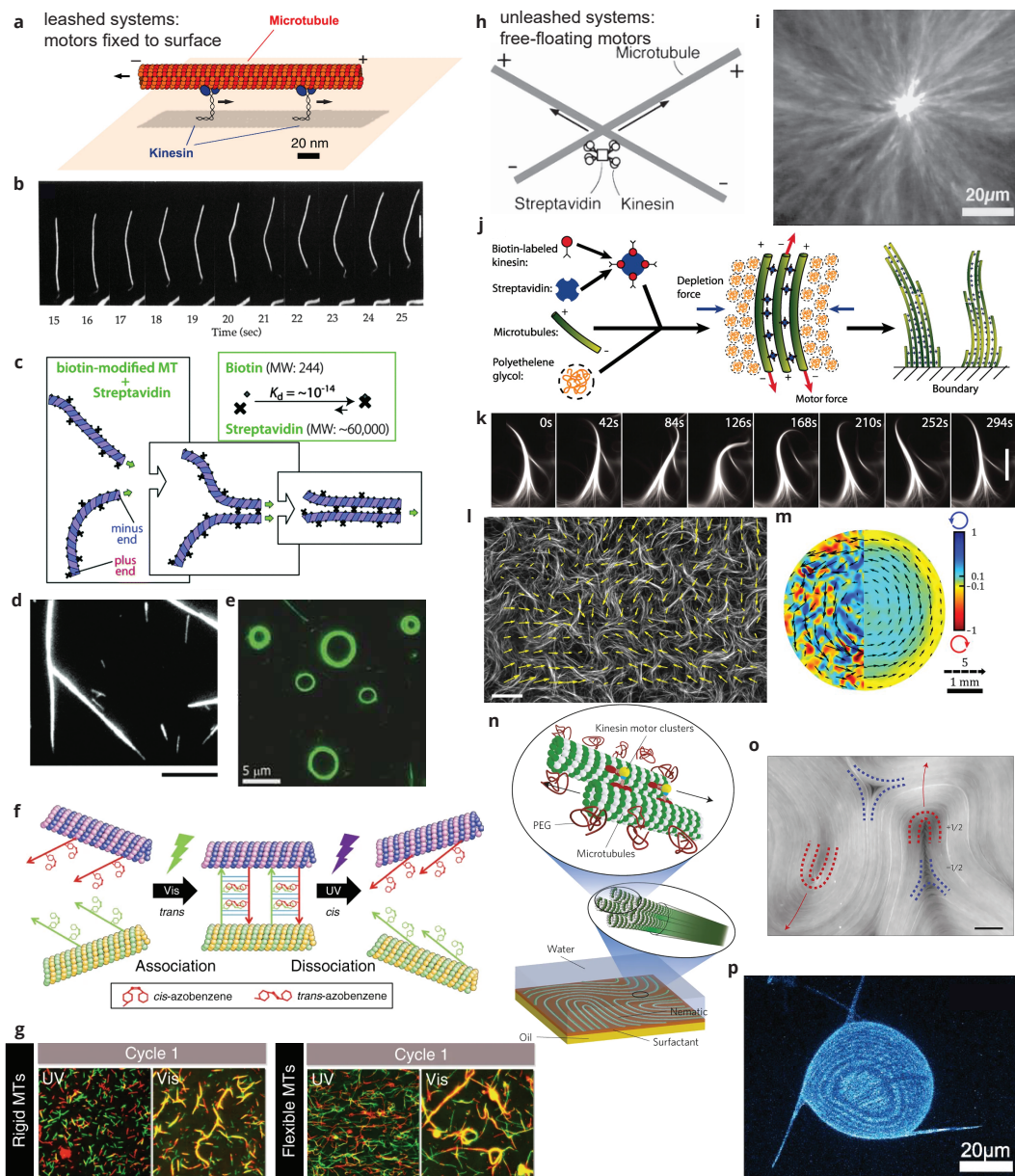


Figure 1.1 (*previous page*): An overview of artificial leashed and unleashed motor-filament systems. **a**, Schematic for a basic leashed system or gliding assay, where motor proteins are attached to a surface and propel filaments adapted from [15]. **b**, Fluorescence microscopy time lapse of a gliding filament from [16]. Bar is 10  $\mu\text{m}$ . **c**, Schematic of gliding filaments that directly bind to each other through a biotin-streptavidin bond from [17]. **d**, Fluorescence microscopy image of gliding filaments forming a bundle adapted from [18]. Bar is 20  $\mu\text{m}$ . **e**, Filaments with reduced rigidity are bent into loops from [19]. **f**, Schematic of gliding filaments that form bonds under light control through DNA-azobenzene links from [20]. **g**, The formation of filament bundles and loops under optical control adapted from [20]. **h**, A schematic for a basic unleashed motor-filament system where motors are crosslinked through a biotin-streptavidin bond and drive the filament plus ends together from [21]. **i**, Darkfield microscopy image of filaments organized into an aster. First engineered motor-filament system from [21]. **j**, Illustration showing how the introduction of a depletion agent causes filaments to bundle together from [22]. **k**, Time series of a filament bundle beating at an interface from [22]. Bar is 30  $\mu\text{m}$ . **l**, An active gel generates a turbulent flow field from [23]. Bar is 80  $\mu\text{m}$ . **m**, Flow fields in an active gel are mediated by boundary conditions from [24]. Left and right halves are instant and time-averaged plots, respectively. **n**, Scheme for creating an active nematic where the interplay between the depletion force and the oil layer cause filaments to organize into a nematic phase on a 2D surface from [25]. **o**, Microscopy image showing the movement of topological defects in the filament nematic adapted from [25]. Bar is 50  $\mu\text{m}$ . **p**, Image of an active nematic confined to a vesicle, where four protrusions are formed by topological defects adapted from [26].

In leashed systems, multiple motors bind to a filament and push the filament towards its minus end (Fig. 1.1a). The underlying principle of the leashed system is that the collective binding and pushing of motor proteins cause the filament to glide along the surface at a near constant speed. For motor proteins that lack cooperativity, such as kinesin-1, the speed of a gliding filament is the average motor speed. For Chapters 2 and 3, it is important to highlight that this principle of filaments gliding at the average motor speed applies to any motor density above a certain threshold [27]. Although microtubule filaments have a persistence length on the order of millimeters, the trajectory of a gliding filament can diverge from a straight line due to the motor binding forces (Fig. 1.1b).

A dilute system of gliding filaments on its own does not self-organize into larger structures. However, modifying microtubules so they stick to each other upon collision makes it possible for filament bundles or spinning loops to form. The principle driving self-organization in this case is the introduction of a strong interaction be-

tween gliding filaments. More specifically, microtubules are able to bind to each other through the introduction of biotin-streptavidin binding sites (Fig. 1.1c). Rigid filaments that have been stabilized with GMPCPP will form dense gliding bundles (Fig. 1.1e), while flexible taxol stabilized filaments form spinning loops (Fig. 1.1e). It should be noted that, even without biotin-streptavidin bonds, loops or vortices can be formed at high filament densities [28]. In the high filament density regime, loop formation is driven by the frequent collisions that occur between filaments.

The use of biotin-streptavidin bonds to form gliding bundles or spinning loops makes these self-organization events both spontaneous and irreversible. It is possible, however, to make these structures transient instead of permanent. Transient self-organization is achieved by making the interaction rules between filaments time-dependent. In a recent work, the interactions between filaments was placed under temporal control through DNA-azobenzene bonds (Fig. 1.1f). Filaments are decorated with single stranded DNA containing azobenzene groups. In the off-state, the azobenzenes make DNA hybridization between filaments unfavorable. However, once the azobenzenes are exposed to 480 nm light, DNA hybridization becomes favorable, causing the filaments to stick to each other. Consequently, it is possible to toggle the formation of gliding bundles or loops by exposing the system to light (Fig. 1.1g). Although the interactions between filaments is controlled optically, there is no evidence that there is spatial localization of the filament interactions. Part of the challenge with using the azobenzene switch is that the dissociation of the DNA bonds is on the order of tens of minutes, which limits the possibility to localize self-organization in space and time.

I now will focus on principles of self-organization in unleashed motor-filament systems, where motors are free-floating in the solution. In the unleashed setting, an individual motor no longer has a fixed surface to press off of and do work on a filament. As a result, the presence of motors in a sample of free-floating proteins is indistinguishable based on the movements of filaments under a microscope. However, motors can be linked together through a biotin-streptavidin bond, which causes clustered motors to pull on each other as they translate towards their filament's plus end (Fig. 1.1h). This is the key principle of the unleashed system: strong interactions between motor proteins drives the organization of microtubules. In a bulk mixture of filaments and linked motors, filament plus ends are drawn together to form a radially symmetric aster structure (Fig. 1.1i). The motor distribution also increases at the aster center since the filament plus ends are all pointing towards the

aster center [29]. Like the unleashed system, it is possible to make the interactions between motor proteins time-dependent in order to make aster formation a transient event. This has been demonstrated by controlling the interaction between motor proteins through DNA strand displacement reactions [30].

In the case of aster self-organization, the dominant interaction between microtubules is mediated through motor protein bonds. Therefore, the properties of the motors will determine how microtubules are self-organized. A striking example of this principle is demonstrated through the addition of minus-directed motor clusters. A mixture of plus and minus directed motor clusters will self-organize into a network of plus and minus centered asters [31].

A strong attractive bond between motors of the same polarity results in a contractile force, where the plus ends of microtubules are drawn together. Large-scale extensile motion between filaments can instead be created by increasing the steric interactions between filaments. The continuous reorganization of tightly packed filaments underlies several self-organizing phenomena. The role of direct filament interactions in self-organization can be achieved through the addition of a depletion agent, such as PEG (polyethylene glycol). The presence of many small inert particles diffusing through a solution crowd the filaments so that the filaments bundle together (Fig. 1.1j). In the presence of a depletion force, it is no longer energetically favorable for motor proteins to pull the plus ends of filaments together. Instead, filaments are shuffled along the bundles. In the case of flexible filaments, bundles that form along a solid surface will wave back and forth in an oscillatory manner (Fig. 1.1k). The mechanism of these oscillations is unclear, but it is speculated that filaments are bent by clusters of anti-parallel filaments. For rigid filaments, the presence of a depletion force results in turbulent flows that are formed as filaments slide back and forth against each other (Fig. 1.1l).

The turbulent flows generated by this active gel are chaotic. However, recent work has shown that it is possible to generate coherent flows through the boundaries of the sample chamber. Here is an important principle, that the geometry of a boundary can influence the behavior of a self-organized system. By confining the system to a cylindrical or toroidal chamber, it is possible to generate clockwise or counterclockwise flow patterns (Fig. 1.1m). Dynamic structures can also be formed by imposing stronger boundary conditions on the system, which is achieved by forcing the filaments onto a 2D surface. A 2D sheet of filaments is made through electrostatic interactions, where filaments pack onto the surface of an oil layer. The

filament density on this oil layer is sufficiently high that they locally align with each other, forming a nematic (Fig. 1.1n). Within this nematic are defects, that is, there are regions where the filament alignment is undefined. These defects can be assigned a topological charge, which is defined by the net phase of a closed path enclosing the defect (this is the same principle that Gauss's Law uses for calculating a net charge).

The topological defects are an example of a type of dynamic structure that can arise by confining filaments that have mesoscopic interaction rules. In the case of the nematic, there are two types of topological defects that form:  $+1/2$  and  $-1/2$ . With the introduction of clustered motors, the location of defects move throughout the nematic as filaments shuffle against each other (Fig. 1.1o). When  $+1/2$  and  $-1/2$  defects collide, they annihilate, but new defects will spontaneously form within the system. Like the active gel, it is also possible to control the total number of defects in an active nematic through boundary conditions. For example, an active nematic confined to the inner shell of a sphere will form four defects that oscillate between two distinct configurations. The topological defects are also an example of a self-organized structure that carries distinct mechanical properties. Defects are the highest regions of stress within a nematic. As a result, it has been possible to use topological defects to generate protrusions on an elastic membrane (Fig. 1.1p).

In this overview, it is clear that leashed and unleashed artificial systems are able to self-organize into a variety of dynamic structures. However, without the presence of boundary conditions, the self-organized structures form spontaneously and randomly. This stands in stark contrast to living cells, where structures self-organize at specific locations and times through the spatiotemporal regulation of motor and filament interactions. This broken symmetry is achieved in living matter through chemical signals that vary in space and time. Patterned chemical signals enable prokaryotic cells to establish their centers during division and is the basis by which eukaryotic cells polarize and follow chemical gradients, for example. How self-organization depends on spatiotemporal boundary conditions remains unknown both in experiment and theory because the ability to pattern activity is largely absent from artificial motor-filament systems. In Chapter 2, I show new self-organization behaviors that arise by localizing motor-filament activities in space and time. I show that asters form, move, interact, and generate advective fluid flows in response to dynamic patterns of motor linking.

### 1.2.1 Spatial-Temporal Organization of Molecular Interactions

This section provides a few examples of how cells enforce spatiotemporal boundary conditions over mechanical processes.

A classical molecular system with temporal variation is the Kai protein oscillator that acts as the circadian clock in cyanobacteria [32]. The Kai circadian clock is responsible for the timing of mechanical events like cell division and the compaction of chromosome [33]. The system is composed of four components: the proteins KaiA, KaiB, and KaiC, and chemical fuel from ATP. While the interactions are somewhat complicated [34] the simplified scheme is as follows. KaiC can undergo both autophosphorylation and autodephosphorylation, KaiA enhances KaiC's autophosphorylation, while KaiB suppresses KaiA. When the purified components are combined together in equal quantities, the amount of phosphorylated KaiC oscillates over a 24 hour period. It is worth restating that these oscillations occur within a well mixed bulk solution, and there is no discernible spatial variability. In this sense, the Kai system is purely a temporal oscillator. The Kai scheme is an example of a reaction diffusion system. In a standard reaction diffusion system, the local concentration of a chemical species is defined by its chemical reaction network and the diffusion kinetics of the molecules.

In contrast to the Kai scheme, an archetypal spatial molecular oscillator is the Min system [35]. Bacteria use the waves generated on the membrane surface to identify the cell's center. Once the cell's center is designated by the Min proteins, a filamentous ring forms that contracts to bisect the cell during division. The general scheme of the Min system is as follows. MinD:ATP preferentially binds to the membrane where MinD:ATP is already bound. MinE binds to membrane-bound MinD:ATP and phosphorylates the ATP, causing MinD:ADP to release from the membrane. The free-floating MinD:ADP undergoes a nucleotide exchange, converting to MinD:ATP. For a more detailed description see [36]. The reaction dynamics of the Min system results in waves along the membrane's surface, but how can this phenomenon reliably localize its center? The ellipsoidal boundary of the cell stabilizes waves that move along the cell's major axis [37]. It is ultimately the geometry of the membrane that selects for waves that will identify the cell's center.

Eukaryotic cell migration also depends on waves of protein activity along the membrane surface, which lead to the nucleation of actin polymerization [38]. However, these waves are also regulated by the states of membrane receptors, allowing for cells to move according to external cues [39]. Cells use membrane receptor signals to

polarize, establishing a leading edge where actin polymerizes and a tail end where actin depolymerizes. Cell polarization in response to external signals allows for cells to, for example, move up chemical gradients. The fact that membrane signals guide the self-organization of the cytoskeleton has been exploited to make cells migrate in response to artificial signals. For example, cells have been made to move in response to light by fusing membrane signaling proteins to optogenetic proteins, which form reversible heterodimers under light excitation [40, 41].

Cells also use compartments to localize molecules or nucleate reactions. One of the best examples of this are clathrin coated vesicles, which transport molecular cargo between the outside of the cell and organelles [42]. More recently there has been an interest in phase separated condensates made of proteins and RNA, which behave as membraneless compartments [43]. A condensate forms through the weak attractions between its constituent molecules, forming a droplet with liquid or gel-like properties.

In the cell, phase separated condensates appear to have a variety of roles, but a prime example is the centrosome [44]. The pericentriolar material, which is part of the centrosome, forms an amorphous condensate that recruits tubulin nucleating proteins. The recruitment of nucleating factors to the centrosome results in the formation of microtubule spindles. Centrosomes break symmetry by localizing spindle formation to opposite poles of the cell and also determine the number of spindles that form. Another example of phase separated condensates regulating a mechanical process is T-cell receptor activation. When T-cell receptors are activated, a phase separated condensate forms that nucleates the polymerization of actin filaments at the cell membrane [45].

Spatial and temporal variation in chemical and mechanical activity makes it possible for living systems to perform essential mechanical tasks. How self-organizing systems respond to boundary conditions that vary in space and time remains unclear because we lack experimental tools for implementing such boundary conditions. The mechanisms the cell uses for localizing mechanical activity in space and time is challenging to implement experimentally, requiring interactions with receptors, lipid membranes, and complexes of many proteins. The reconstitution of T-cell receptor signal transduction, for example, required 12 purified components. If we are to distill the effects of the boundary conditions on active self-organization, it will be necessary to develop a simple method to impose arbitrary patterns of activity.

### 1.2.2 Molecular and Experimental Details of the Microtubule-Kinesin System

In this section I focus on the molecular details of unleashed systems containing microtubule filaments and kinesin motors. Microtubules have a diameter of 25 nm and are usually grown to an average length of  $\approx 5 \mu\text{m}$  (except for the case of the active nematic, where filaments are grown to  $1 \mu\text{m}$  [23]). Microtubules are rigid compared to other biopolymers, having a persistence length of 1.4  $\mu\text{m}$  [46]. The visualization of microtubules is typically achieved by mixing a small population of fluorescently labeled tubulin into a tube of unlabeled tubulin before polymerization. It should be noted that motor-filament interactions diminish when microtubules contain higher proportions of labeled tubulin [47]. Microtubules are stabilized by either polymerizing tubulin with a non-hydrolyzable form of GTP such as GMPCPP, or the addition of a small molecule stabilizing agent called taxol. While earlier works used taxol for stabilization, more recent papers have stabilized microtubules with GMPCPP. The persistence length of taxol stabilized filaments is approximately half that of GMPCPP and non-stabilized microtubules [48]. In addition, it has been observed that taxol-stabilized microtubules have a tendency to bundle together [49]. It is therefore extremely important to take the stabilization method into account when comparing results between experiments. Although tubulin is evolutionarily conserved [50], the source of tubulin can impact experiments due to post-translational modifications and tubulin isoforms. Microtubules are typically sourced from bovine or porcine brains because of the high yield they offer. However, the modifications and types of tubulin differ across species and cell types. These differences are known to affect motor speed and run length [51].

The relationship between self-organization and the properties of motor proteins is similarly complex. The motor that is most commonly used in microtubule experiments is *Drosophila melanogaster* kinesin-1. Full length kinesin-1 is  $\approx 60 \text{ nm}$  in size [52] and has an average speed of 800 nm/s [53]. The step size of the motor is 8 nm and takes an average of 150 steps before falling off from a microtubule [53]. The stall force is approximately 5 pN [54]. As to whether or not kinesin-1 dwells at the end of a microtubule or immediately falls off remains a point of contention. While certain motors do end-dwell, there is no direct evidence to indicate that kinesin-1 end dwells. However, simulations (unpublished data from simulations I ran and independent work by Sebastian Fürthauer) suggest that aster formation should not be possible without end dwelling. To see why this is, picture two microtubules pointing in the same direction and aligned with the x-axis. Further, the plus ends of these microtubules are slightly offset from each other in x. If a motor falls off

right when it reaches the plus end, then these microtubules will never experience a translational force that will bring the two plus ends together. See Fig. 4 in [55] for a more detailed illustration. An alternative possibility is the presence of dead motors, which bind to microtubules but do not walk. These dead motors may add a friction term that makes aster formation possible. What fraction of motors are dead and exactly how dead motors might influence self-organization is presently unknown. The behaviors of motors have also been shown to depend on how they are expressed. Even genetically identical kinesin-1 expressed in bacteria or in insect cells have shown notable differences in behavior [56]. The hypothesis is that bacteria produce a non-motile motor sub-population due to premature translation termination, but it has not been explicitly tested. Since kinesin-1 is a motor that is native to insect cells, perhaps there are post-translational modifications that do not occur when kinesin-1 is expressed in bacteria. In spite of evidence that insect cells produce more robust motors, most works rely on bacterial expression because it can be faster, easier, more cost effective, and produces higher protein yields than insect cell purification.

An extremely important, yet often underappreciated challenge of working with purified protein systems is surface passivation. In order to look at the protein mixtures under a microscope, the mixture must be placed into a glass chamber. Proteins, however, have a tendency to adsorb onto glass surfaces due to electrostatics and hydrophobic interactions [57]. Surfaces that are insufficiently passivated will sequester motors and pull asters apart. It is therefore necessary to modify the surface of the glass chambers in order to prevent motor adsorption. As one might deduce from Nédélec and Surrey's offer of a fine bottle of red wine to whoever improves the method for passivating and storing glass slides [58], passivation can be a challenging process. It is worth noting that the effectiveness of a passivation technique depends on the proteins being used and should therefore be considered on a case-by-case basis. A simple approach is to coat the glass with another protein in advance, such as bovine serum albumin or casein. However, these proteins will not create a continuous coating nor do they covalently bind to the glass surface, so any initial passivation effect may decay over time. An alternative solution is to chemically modify the glass surface by forming a hydrophilic brush. Typically, a layer of PEG is covalently linked to a silanized glass surface [59]. While effective, the process of forming a PEG brush is time consuming and is difficult to store due to PEG-silane's susceptibility to hydrolysis [60]. For the kinesin-microtubule system, the most robust passivation protocol is the generation of an acrylamide brush [61],

which is also time consuming, but is stable in room temperature water for months.

In the development of the system introduced in Chapter 2, it was necessary to decide how to stabilize microtubules, what motors to use, and how to passivate the sample chamber. Initially, taxol stabilized microtubules were used, but *complete* aster disassembly was hindered or possibly absent due to the tendency for taxol stabilized microtubules to stick together. Instead, GMPCPP stabilized microtubules were later used where this bundling behavior is less pronounced. Tubulin was sourced from bovine brain because it is cost effective and standard for most purified tubulin experiments. A truncated form of *Drosophila* kinesin-1, K401, was chosen primarily for historical reasons. Since the first artificial aster paper [21], all unleashed microtubule systems have used this motor for self-organization. For surface passivation, the first scheme that showed promise was the PEG-silane chemistry. However, in my hands, the passivation was inconsistent and decayed within a few days of storage. For the finalized protocol, I decided to use the acrylamide passivation chemistry because it was much more robust relative to PEG-silane. Another essential feature in the experimental system is the presence of an energy recycling system. Without a way to recycle ADP back into ATP, the unleashed motor-filament system will run out of energy to power the motors on the order of minutes. For this reason, I used the same pyruvate-kinase recycling system as has been used in other unleashed motor-filament systems [23]. Some of these choices may seem arbitrary, and indeed some quick decisions were made because the parameter space here is quite large. There is certainly a lot of room to explore how the properties of microtubules and motors determine mesoscopic behaviors of the unleashed system.

### 1.2.3 Modeling the Kinesin-Microtubule System

In this section, I will provide a very brief overview of how motor-filament interactions are modeled. Models of the leashed and unleashed systems share the same basic aspects. Filaments are treated as thin rods with a center of mass  $\mathbf{x}$  and orientation  $\mathbf{p}$ . Filaments interact with each other through motor cross-links. The equation of motion for a single filament is

$$m\ddot{\mathbf{x}} = F^{\text{mot}} + F^{\text{fluid}} \quad (1.1)$$

where  $m$  is the mass of the filament,  $F^{\text{mot}}$  is the force exerted on the filament by the motor interactions, and  $F^{\text{fluid}}$  are the forces that come from the solvent such as the viscous drag, fluid flow, and thermal fluctuations. A similar equation can be written

for the torque. The inertial terms in the motor-filament system are much less than the viscous terms, making this a low Reynolds number problem. In other words, if a particle were to stop generating a propulsive force (and undergo no thermal motion), it would coast a fraction of an angstrom before it would stop moving [62]. Consequently, the left side of the above equation can be approximated to be equal to zero, i.e.  $F^{\text{total}} = 0 \rightarrow F^{\text{mot}} = -F^{\text{fluid}}$ . In the case of a dense field of microtubules, it is important to also account for the steric interactions between filaments, which is responsible for the alignment seen in the nematic phase [63].

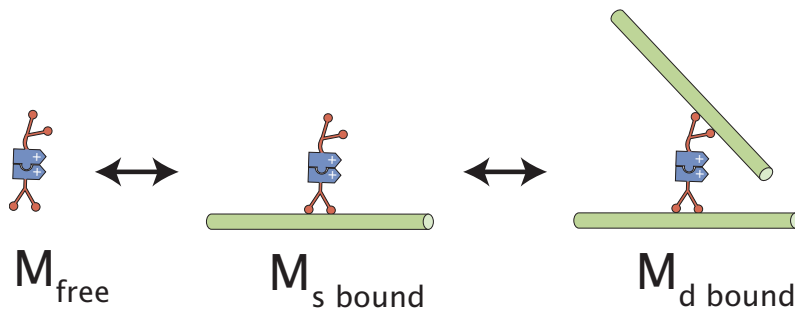
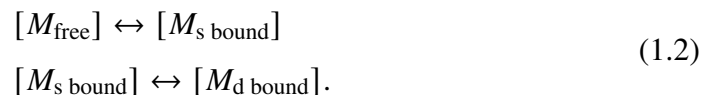


Figure 1.2: Schematic of motor binding dynamics

In the unleashed systems, motors are clustered together through biotin-streptavidin links. For simplicity, I will designate each motor cluster as containing two motor complexes (this is not exactly the case experimentally [21]). Although a single motor complex has two microtubule binding domains, I will assume that a single motor can only bind to one microtubule at a time due to the geometry of the motor proteins. There are effectively three populations of motors in the system: free, single bound, and double bound (Fig. 1.2):



The motion of a free motor is dictated by thermal fluctuations and fluid flow until it binds to a filament. A single bound motor cluster will move towards a filament's plus end at the motor's unloaded step speed. These motors will eventually come off the microtubule as dictated by the motor's processivity and end-dwelling properties. The position of a bound motor can be written relative to the filament's centroid as  $\mathbf{x} + s\mathbf{p}$ . Further, a single bound motor can be approximated as attributing no net force to a filament as it moves. When a motor cluster binds to two filaments, however, an equal and opposite force is applied through the crosslink as both motors move

towards the filament plus ends. The speed at which double bound motors move is a function of the amount of force applied to them [54]. Similarly, motor processivity decays as a function of the force [64].

Motors cause filaments to slide across each other through pairwise crosslinks,  $F_{ij}^{\text{mot}} = -F_{ji}^{\text{mot}}$ . This provides a force balance requirement  $\sum F^{\text{mot}} = 0$ . In the case of a highly crosslinked network, it can be argued that the force contributions due to fluid flow are negligible [65]. However, this approximation is not valid for all self-organizing motor filament systems, as will become apparent in Chapter 2. When including fluid interactions, the drag force on a microtubule can be calculated based on the slender body approximation. The movement of the filaments will induce a stress in the fluid as described by a force-free Stokes flow. It is worth noting that the treatment of microtubules as rigid rods will fail to capture some phenomena, such as the ring patterns formed during gliding assays [66, 67].

Models of motor-filament systems are still in their early stages. There have so far been no major “figure 1 models” (a term coined by Rob Phillips), where the predictions of a model are used to motivate experiment. One challenge to modeling motor-filament systems is that organization spans multiple length scales. Capturing the details of nanometer-scale interactions and carrying them across to the micrometer length scale is computationally expensive. Computational costs are further exacerbated by the inclusion of hydrodynamic interactions. Advancements in coarse analytical models similar to [65] and numerical simulations frameworks like cytosim [68] or finite element modelling will be necessary for a figure 1 model to come to fruition.

## References

1. Levine, H. & Rappel, W.-J. The physics of eukaryotic chemotaxis. *Physics Today* **66**, 24–30. doi:10.1063/pt.3.1884 (2013).
2. Blakemore, R. P. Magnetotactic bacteria. *Annual Reviews in Microbiology* **36**, 217–238 (1982).
3. Harland, B., Walcott, S. & Sun, S. X. Adhesion dynamics and durotaxis in migrating cells. *Physical Biology* **8**, 015011. doi:10.1088/1478-3975/8/1/015011 (2011).
4. Ramaswamy, S. Active matter. *Journal of Statistical Mechanics: Theory and Experiment* **2017**, 054002 (2017).

5. Battle, C., Broedersz, C. P., Fakhri, N., Geyer, V. F., Howard, J., Schmidt, C. F. & MacKintosh, F. C. Broken detailed balance at mesoscopic scales in active biological systems. *Science* **352**, 604–607 (2016).
6. England, J. L. Dissipative adaptation in driven self-assembly. *Nature Nanotechnology* **10**, 919 (2015).
7. Wolfram, S. Computation theory of cellular automata. *Communications in Mathematical Physics* **96**, 15–57 (1984).
8. Woods, D., Chen, H.-L., Goodfriend, S., Dabby, N., Winfree, E. & Yin, P. Active Self-Assembly of Algorithmic Shapes and Patterns in Polylogarithmic Time. *arXiv preprint arXiv:1301.2626* (2013).
9. Chen, M., Xin, D. & Woods, D. Parallel computation using active self-assembly. *Natural Computing* **14**, 225–250 (2015).
10. Malumbres, M. & Barbacid, M. Cell cycle, CDKs and cancer: A changing paradigm. *Nature Reviews Cancer* **9**, 153–166 (2009).
11. Rothmund, P. W. K. Folding DNA to create nanoscale shapes and patterns. *Nature* **440**, 297–302. ISSN: 1476-4687. doi:10.1038/nature04586 (2006).
12. Tikhomirov, G., Petersen, P. & Qian, L. Fractal assembly of micrometre-scale DNA origami arrays with arbitrary patterns. *Nature* **552**, 67–71. ISSN: 1476-4687. doi:10.1038/nature24655 (2017).
13. Gopinath, A., Miyazono, E., Faraon, A. & Rothmund, P. W. K. Engineering and mapping nanocavity emission via precision placement of DNA origami. *Nature* **535**, 401–405. doi:10.1038/nature18287 (2016).
14. Bazrafshan, A., Meyer, T. A., Su, H., Brockman, J. M., Blanchard, A. T., Piranej, S., Duan, Y., Ke, Y. & Salaita, K. Tunable DNA Origami Motors Translocate Ballistically Over  $\mu\text{m}$  Distances at nm/s Speeds. *Angewandte Chemie International Edition*. doi:10.1002/anie.201916281 (2020).
15. Diez, S., Helenius, J. H. & Howard, J. in *Nanobiotechnology* 185–199 (Wiley-VCH Verlag GmbH & Co. KGaA, 2005). doi:10.1002/3527602453.ch13.
16. Ray, S., Meyhöfer, E., Milligan, R. A. & Howard, J. Kinesin follows the microtubule's protofilament axis. *The Journal of Cell Biology* **121**, 1083–1093 (1993).
17. Kawamura, R., Kakugo, A., Shikinaka, K., Osada, Y. & Gong, J. P. Formation of motile assembly of microtubules driven by kinesins. *Smart Materials and Structures* **20**, 124007 (2011).
18. Kawamura, R., Kakugo, A., Osada, Y. & Gong, J. P. Selective formation of a linear-shaped bundle of microtubules. *Langmuir* **26**, 533–537 (2010).
19. Liu, H., Spoerke, E. D., Bachand, M., Koch, S. J., Bunker, B. C. & Bachand, G. D. Biomolecular motor-powered self-assembly of dissipative nanocomposite rings. *Advanced Materials* **20**, 4476–4481 (2008).

20. Keya, J. J., Suzuki, R., Kabir, A. M. R., Inoue, D., Asanuma, H., Sada, K., Hess, H., Kuzuya, A. & Kakugo, A. DNA-assisted swarm control in a biomolecular motor system. *Nature Communications* **9**, 453. ISSN: 2041-1723. doi:10.1038/s41467-017-02778-5 (2018).
21. Nédélec, F. J., Surrey, T., Maggs, A. C. & Leibler, S. Self-organization of microtubules and motors. *Nature* **389**, 305. ISSN: 1476-4687. doi:10.1038/38532 (1997).
22. Sanchez, T., Welch, D., Nicastro, D. & Dogic, Z. Cilia-Like Beating of Active Microtubule Bundles. *Science* **333**, 456–459. ISSN: 0036-8075, 1095-9203. doi:10.1126/science.1203963 (2011).
23. Sanchez, T., Chen, D. T. N., DeCamp, S. J., Heymann, M. & Dogic, Z. Spontaneous motion in hierarchically assembled active matter. *Nature* **491**, 431. ISSN: 1476-4687. doi:10.1038/nature11591 (2012).
24. Wu, K.-T., Hishamunda, J. B., Chen, D. T. N., DeCamp, S. J., Chang, Y.-W., Fernández-Nieves, A., Fraden, S. & Dogic, Z. Transition from turbulent to coherent flows in confined three-dimensional active fluids. *Science* **355**, eaal1979. ISSN: 0036-8075, 1095-9203 (2017).
25. DeCamp, S. J., Redner, G. S., Baskaran, A., Hagan, M. F. & Dogic, Z. Orientational order of motile defects in active nematics. *Nature Materials* **14**, 1110. ISSN: 1476-4660. doi:10.1038/nmat4387 (2015).
26. Keber, F. C., Loiseau, E., Sanchez, T., DeCamp, S. J., Giomi, L., Bowick, M. J., Marchetti, M. C., Dogic, Z. & Bausch, A. R. Topology and dynamics of active nematic vesicles. *Science* **345**, 1135–1139. ISSN: 0036-8075, 1095-9203. doi:10.1126/science.1254784 (2014).
27. Hancock, W. O. & Howard, J. Processivity of the Motor Protein Kinesin Requires Two Heads. *Journal of Cell Biology* **140**, 1395–1405. doi:10.1083/jcb.140.6.1395 (1998).
28. Sumino, Y., Nagai, K. H., Shitaka, Y., Tanaka, D., Yoshikawa, K., Chaté, H. & Oiwa, K. Large-scale vortex lattice emerging from collectively moving microtubules. *Nature* **483**, 448–452 (2012).
29. Nédélec, F., Surrey, T. & Maggs, A. C. Dynamic Concentration of Motors in Microtubule Arrays. *Physical Review Letters* **86**, 3192–3195. doi:10.1103/PhysRevLett.86.3192 (2001).
30. Wollman, A. J. M., Sanchez-Cano, C., Carstairs, H. M. J., Cross, R. A. & Turberfield, A. J. Transport and self-organization across different length scales powered by motor proteins and programmed by DNA. *Nature Nanotechnology* **9**, 44–47. doi:10.1038/nnano.2013.230 (2013).
31. Surrey, T., Nédélec, F., Leibler, S. & Karsenti, E. Physical Properties Determining Self-Organization of Motors and Microtubules. *Science* **292**, 1167–1171. ISSN: 0036-8075, 1095-9203. doi:10.1126/science.1059758 (2001).

32. Nakajima, M., Imai, K., Ito, H., Nishiwaki, T., Murayama, Y., Iwasaki, H., Oyama, T. & Kondo, T. Reconstitution of circadian oscillation of cyanobacterial KaiC phosphorylation in vitro. *Science* **308**, 414–415 (2005).
33. Cohen, S. E. & Golden, S. S. Circadian Rhythms in Cyanobacteria. *Microbiology and Molecular Biology Reviews* **79**, 373–385. doi:10.1128/mmbr.00036-15 (2015).
34. Markson, J. S. & O’Shea, E. K. The molecular clockwork of a protein-based circadian oscillator. *FEBS Letters* **583**, 3938–3947 (2009).
35. Loose, M., Kruse, K. & Schwille, P. Protein self-organization: Lessons from the min system. *Annual Review of Biophysics* **40**, 315–336 (2011).
36. Huang, K. C. & Wingreen, N. S. Min-protein oscillations in round bacteria. *Physical Biology* **1**, 229 (2004).
37. Zieske, K. & Schwille, P. Reconstitution of self-organizing protein gradients as spatial cues in cell-free systems. *eLife* **3**, e03949 (2014).
38. Inagaki, N. & Katsuno, H. Actin waves: Origin of cell polarization and migration? *Trends in Cell Biology* **27**, 515–526 (2017).
39. Graziano, B. R. & Weiner, O. D. Self-organization of protrusions and polarity during eukaryotic chemotaxis. *Current Opinion in Cell Biology* **30**, 60–67 (2014).
40. Wu, Y. I., Frey, D., Lungu, O. I., Jaehrig, A., Schlichting, I., Kuhlman, B. & Hahn, K. M. A genetically encoded photoactivatable Rac controls the motility of living cells. *Nature* **461**, 104–108 (2009).
41. Xu, Y., Hyun, Y.-M., Lim, K., Lee, H., Cummings, R. J., Gerber, S. A., Bae, S., Cho, T. Y., Lord, E. M. & Kim, M. Optogenetic control of chemokine receptor signal and T-cell migration. *Proceedings of the National Academy of Sciences* **111**, 6371–6376 (2014).
42. Robinson, M. S. Forty years of clathrin-coated vesicles. *Traffic* **16**, 1210–1238 (2015).
43. Hyman, A. A., Weber, C. A. & Jülicher, F. Liquid-liquid phase separation in biology. *Annual Review of Cell and Developmental Biology* **30**, 39–58 (2014).
44. Woodruff, J. B., Gomes, B. F., Widlund, P. O., Mahamid, J., Honigsmann, A. & Hyman, A. A. The centrosome is a selective condensate that nucleates microtubules by concentrating tubulin. *Cell* **169**, 1066–1077 (2017).
45. Su, X., Ditlev, J. A., Hui, E., Xing, W., Banjade, S., Okrut, J., King, D. S., Taunton, J., Rosen, M. K. & Vale, R. D. Phase separation of signaling molecules promotes T cell receptor signal transduction. *Science* **352**, 595–599 (2016).
46. Van Mameren, J., Vermeulen, K. C., Gittes, F. & Schmidt, C. F. Leveraging single protein polymers to measure flexural rigidity. *The Journal of Physical Chemistry B* **113**, 3837–3844 (2009).

47. Korten, T. & Diez, S. Setting up roadblocks for kinesin-1: mechanism for the selective speed control of cargo carrying microtubules. *Lab on a Chip* **8**, 1441–1447 (2008).
48. Hawkins, T. L., Sept, D., Mogessie, B., Straube, A. & Ross, J. L. Mechanical properties of doubly stabilized microtubule filaments. *Biophysical Journal* **104**, 1517–1528 (2013).
49. Xiao, H., Verdier-Pinard, P., Fernandez-Fuentes, N., Burd, B., Angeletti, R., Fiser, A., Horwitz, S. B. & Orr, G. A. Insights into the mechanism of microtubule stabilization by Taxol. *Proceedings of the National Academy of Sciences* **103**, 10166–10173 (2006).
50. Ludueña, R. F. in *International Review of Cell and Molecular Biology* 41–185 (Elsevier, 2013).
51. Sirajuddin, M., Rice, L. M. & Vale, R. D. Regulation of microtubule motors by tubulin isoforms and post-translational modifications. *Nature Cell Biology* **16**, 335 (2014).
52. Kerssemakers, J., Howard, J., Hess, H. & Diez, S. The distance that kinesin-1 holds its cargo from the microtubule surface measured by fluorescence interference contrast microscopy. *Proceedings of the National Academy of Sciences* **103**, 15812–15817 (2006).
53. Coy, D. L., Wagenbach, M. & Howard, J. Kinesin takes one 8-nm step for each ATP that it hydrolyzes. *Journal of Biological Chemistry* **274**, 3667–3671 (1999).
54. Svoboda, K. & Block, S. M. Force and velocity measured for single kinesin molecules. *Cell* **77**, 773–784 (1994).
55. Nédélec, F. & Surrey, T. Dynamics of microtubule aster formation by motor complexes. *Comptes Rendus de l'Académie des Sciences - Series IV - Physics-Astrophysics* **2**, 841–847. doi:10.1016/s1296-2147(01)01227-6 (2001).
56. Korten, T., Chaudhuri, S., Tavkin, E., Braun, M. & Diez, S. Kinesin-1 expressed in insect cells improves microtubule in vitro gliding performance, long-term stability and guiding efficiency in nanostructures. *IEEE Transactions on Nanobioscience* **15**, 62–69 (2016).
57. Duncan, M. R., Lee, J. M. & Warchol, M. P. Influence of surfactants upon protein/peptide adsorption to glass and polypropylene. *International Journal of Pharmaceutics* **120**, 179–188 (1995).
58. Nédélec, F. & Surrey, T. in *Kinesin Protocols* 213–222 (Springer, 2001).
59. Chandradoss, S. D., Haagsma, A. C., Lee, Y. K., Hwang, J.-H., Nam, J.-M. & Joo, C. Surface passivation for single-molecule protein studies. *JoVE (Journal of Visualized Experiments)*, e50549 (2014).

60. Gidi, Y., Bayram, S., Ablenas, C. J., Blum, A. S. & Cosa, G. Efficient One-Step PEG-Silane Passivation of Glass Surfaces for Single-Molecule Fluorescence Studies. *ACS Applied Materials & Interfaces* **10**, 39505–39511 (2018).
61. Lau, A. W. C., Prasad, A. & Dogic, Z. Condensation of isolated semi-flexible filaments driven by depletion interactions. *EPL (Europhysics Letters)* **87**, 48006 (2009).
62. Purcell, E. M. Life at low Reynolds number. *American Journal of Physics* **45**, 3–11 (1977).
63. Gao, T., Blackwell, R., Glaser, M. A., Betterton, M. & Shelley, M. J. Multiscale modeling and simulation of microtubule–motor–protein assemblies. *Physical Review E* **92**, 062709 (2015).
64. Thorn, K. S., Ubersax, J. A. & Vale, R. D. Engineering the processive run length of the kinesin motor. *The Journal of Cell Biology* **151**, 1093–1100 (2000).
65. Fürthauer, S., Lemma, B., Foster, P. J., Ems-McClung, S. C., Yu, C.-H., Walczak, C. E., Dogic, Z., Needleman, D. J. & Shelley, M. J. Self-straining of actively crosslinked microtubule networks. *Nature Physics* **15**, 1295–1300 (2019).
66. Liu, L., Tüzel, E. & Ross, J. L. Loop formation of microtubules during gliding at high density. *Journal of Physics: Condensed Matter* **23**, 374104 (2011).
67. Ziebert, F., Mohrbach, H. & Kulić, I. M. Why microtubules run in circles: Mechanical hysteresis of the tubulin lattice. *Physical Review Letters* **114**, 148101 (2015).
68. Sedwards, S. & Mazza, T. Cyto-Sim: a formal language model and stochastic simulator of membrane-enclosed biochemical processes. *Bioinformatics* **23**, 2800–2802 (2007).

*Chapter 2***CONTROLLING ORGANIZATION AND FORCES IN ACTIVE MATTER THROUGH OPTICALLY-DEFINED BOUNDARIES****2.1 Introduction**

Living systems are capable of locomotion, reconfiguration, and replication. To perform these tasks, cells spatiotemporally coordinate the interactions of force-generating, “active” molecules that create and manipulate non-equilibrium structures and force fields that span up to millimeter length scales [1–3]. Experimental active matter systems of biological or synthetic molecules are capable of spontaneously organizing into structures [4, 5] and generating global flows [6–9]. However, these experimental systems lack the spatiotemporal control found in cells, limiting their utility for studying non-equilibrium phenomena and bioinspired engineering. Here, we uncover non-equilibrium phenomena and principles by optically controlling structures and fluid flow in an engineered system of active biomolecules. Our engineered system consists of purified microtubules and light-activatable motor proteins that crosslink and organize microtubules into distinct structures upon illumination. We develop basic operations, defined as sets of light patterns, to create, move, and merge microtubule structures. By composing these basic operations, we are able to create microtubule networks that span several hundred microns in length and contract at speeds up to an order of magnitude faster than the speed of an individual motor. We manipulate these contractile networks to generate and sculpt persistent fluid flows. The principles of boundary-mediated control we uncover may be used to study emergent cellular structures and forces and to develop programmable active matter devices.

**2.2 Optical Control Over Aster Formation**

Our scheme is based on a well-studied active system composed of stabilized microtubule filaments and kinesin motor proteins [4–8, 10–12]. In the original biochemical system, kinesin motors are linked together by practically irreversible biotin-streptavidin bonds. As linked motors pull on microtubules, a variety of phases and structures spontaneously emerge, such as asters, vortices, and networks. However, spatial and temporal control of these structures is limited [5, 13].

We engineered the system so that light activates reversible linking between motors

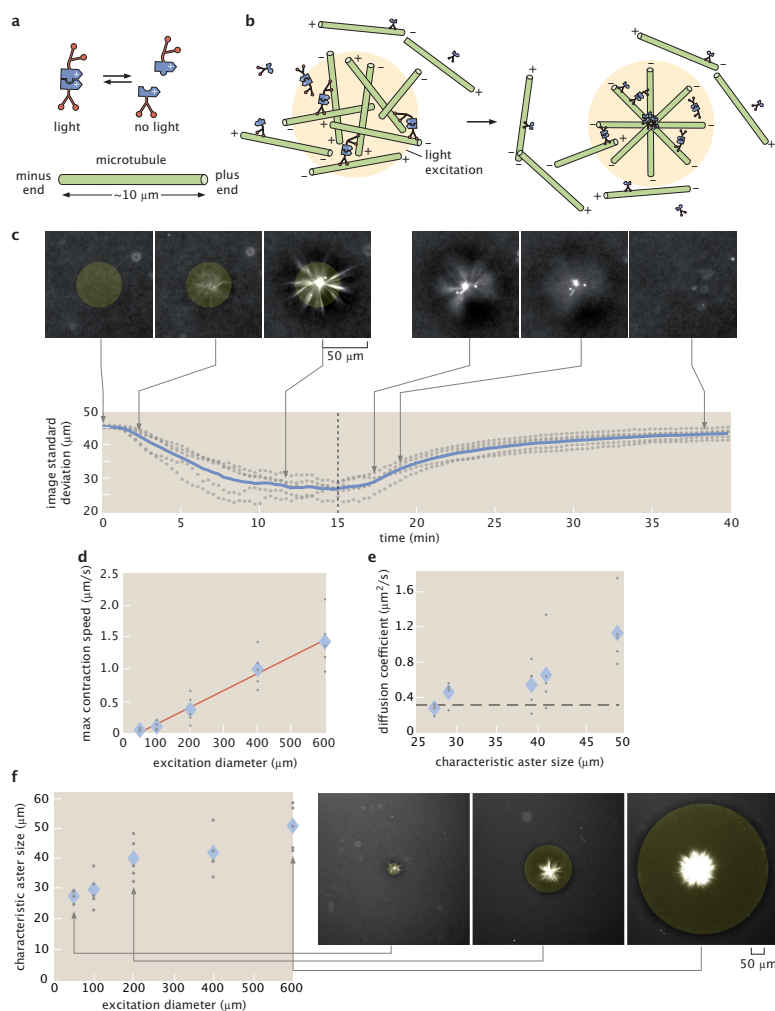


Figure 2.1: Light-switchable active matter system enables optical control over aster formation, decay, and size. **a**, Schematic of light-dimerizable motors. **b**, Schematic of light-controlled reorganization of microtubules into an aster. **c**, Images of labeled microtubules during aster assembly and decay and corresponding image spatial standard deviation versus time. The blue line is the mean of 5 experiments and the gray dots represent individual experiments. The dashed line is when the activation light is removed, transitioning from creation to decay. **d**, Max contraction speed versus excitation diameter. The red line is a linear fit. **e**, Diffusion coefficients versus characteristic aster size. The characteristic size is the image spatial standard deviation at the 15 minute time point shown in (c). The dashed line represents the diffusion coefficient of a  $7 \mu\text{m}$  microtubule (Section 2.2.11). **f**, Aster characteristic size versus excitation diameter with representative images. In (d, e, f), the diamonds represent the mean of 5 experiments and the gray dots represent individual experiments. In (c, f), the yellow shaded disks represent the light pattern.

(Fig. 2.1a) by fusing kinesin-1 motors to optically-dimerizable iLID proteins [14]. Light patterns are projected into the sample throughout its depth and determine when and where motors link. Outside of the light excitation volume, microtubules remain disordered, while inside the light volume, microtubules bundle and organize. The reversibility of the motor linkages allows structures to remodel as we change the light pattern. For a cylinder pattern of light excitation, microtubules contract into a 3D aster (Fig. 2.1b) (Section 2.2.1, Video 1, Video 2). We use the projection of a cylinder of light as an operation for creating asters. We note that vortices, spirals, and extensile behavior are not observed under our conditions (Section 2.2.2).

Our temporal control over aster formation allows us to study the dynamics of their creation and decay (Fig. 2.1c) (Video 3) through time lapse imaging (Section 2.2.3). We characterize these dynamics by measuring the spatial width of the distribution of fluorescently-labeled microtubules using image standard deviation (Section 2.2.4). During aster formation, the distribution of microtubules within a cylinder pattern contracts. After 10-15 min, the distribution reaches a steady state, indicating that the aster is fully formed. To quantify a characteristic aster size (Section 2.2.5), we measure the image standard deviation at 15 min (Section 2.2.6). Once the excitation light is removed, asters begin to decay into free microtubules. The spatial distribution of microtubules widens over time, returning to the initial uniform distribution. Further, aster decay is reversible (Section 2.2.7).

To understand scaling behavior, we investigate how the dynamics of aster formation and decay depend on excitation volume. During formation, microtubule distributions contract. The contraction speed (Section 2.2.8) grows with the diameter of the excitation cylinder (Fig. 2.1d). Similar scaling of contraction speed has been observed for actomyosin systems [15] (Section 2.2.9) and modeled for generic networks [16]. Alternatively, contraction can be measured by a characteristic contraction timescale [17] (see Section 2.2.8). During decay, microtubule distributions spread in a manner consistent with diffusion (Section 2.2.10). The effective diffusion coefficient is independent of characteristic aster size (Fig. 2.1e) and is consistent with what is expected for free microtubules (Section 2.2.11). Further, we manipulate aster size through the diameter of the excitation volume (Fig. 2.1f) and find a scaling dependence (Section 2.2.12) that shows similarities to the dependence of spindle size on confining volumes [18].

### 2.2.1 Aster Distribution in 3D

From z-stack imaging, we observe that asters are complex 3D structures (Fig. 2.2). By analyzing the microtubule density in Z, we find that asters form near the midpoint of the sample plane (Fig. 2.3a). Further, we show that these are symmetric structures by fitting the intensity profiles in the Y plane and Z plane to Gaussians (Fig. 2.3b, c).

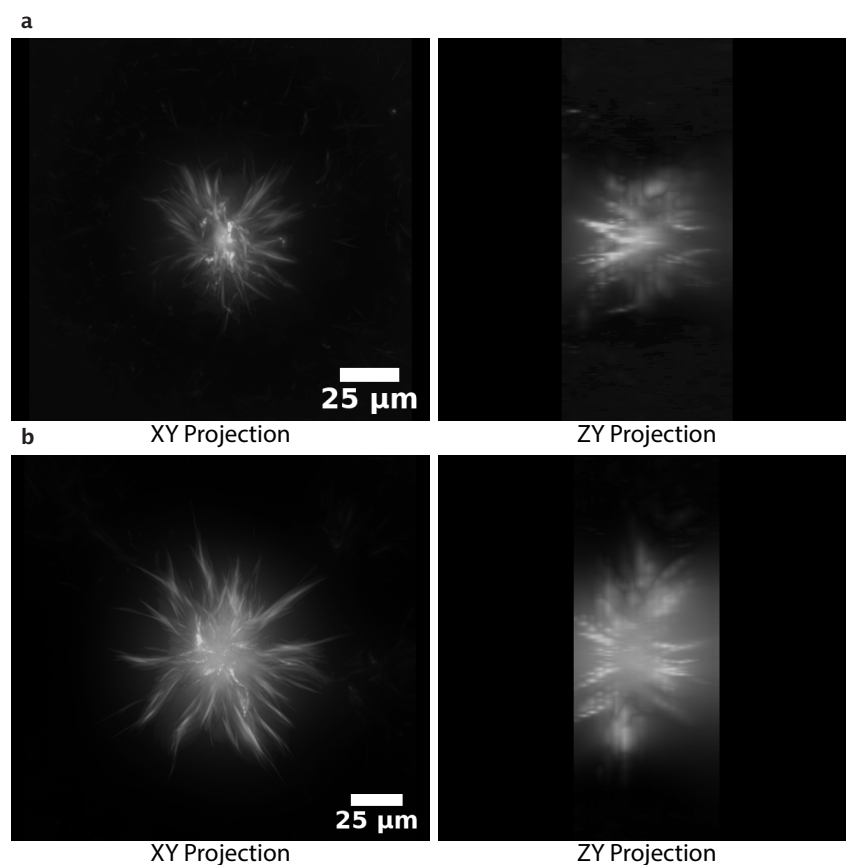


Figure 2.2: 3D projections of asters from z-stacks imaged with a 20x objective. **a**, Aster generated with a 100  $\mu\text{m}$  disk (Video 1). **b**, Aster generated with a 300  $\mu\text{m}$  disk (Video 2). The XY plane is along the plane of the sample slide. The ZY plane is orthogonal to the sample slide and the image is constructed by interpolating over 18 Z-slices spaced by 4  $\mu\text{m}$ .

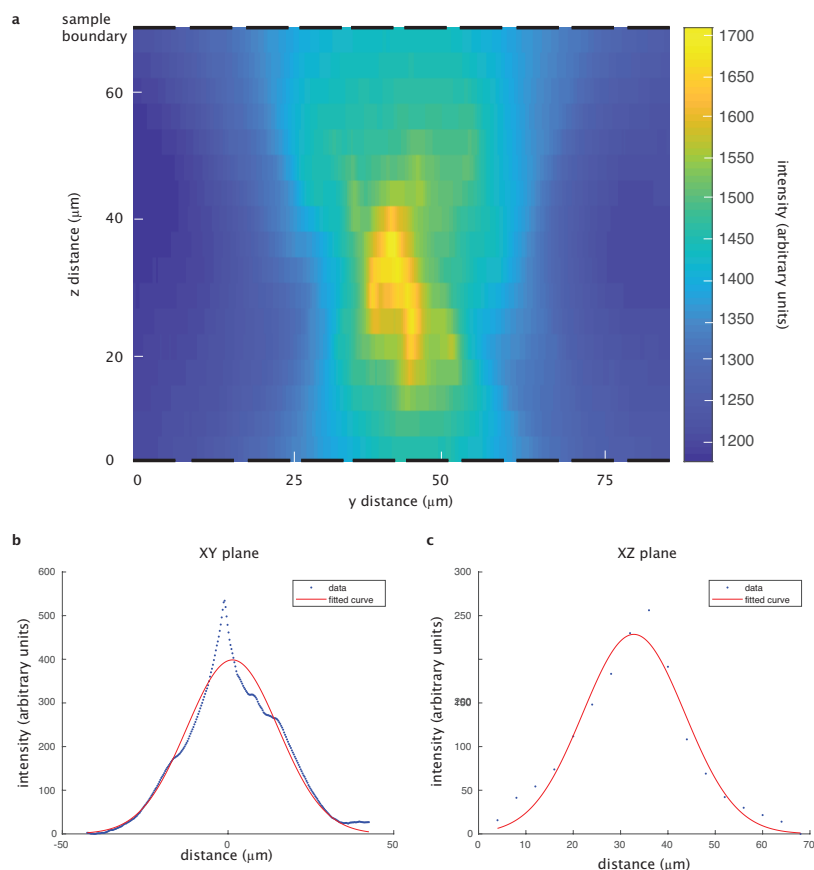


Figure 2.3: Analysis of microtubule distribution in 3D. **a**, Heatmap of microtubule distribution in the YZ plane shown in Fig. 2.2a. Sample boundaries, defined by the coverslips, are denoted by the dashed lines. **b**, Gaussian fit to the microtubule density in the middle slice of the Y plane. **c**, Gaussian fit to the microtubule density along the Z plane.

## 2.2.2 Comparisons with Similar Systems

### Microtubule Vortices

The original microtubule-motor system [4, 5] is contractile and shows the formation of microtubule vortices in addition to asters. Microtubule vortices have not been observed in our experiments, however. This is likely due to the substantial differences between the boundary conditions. Experiments where vortices are reported have a channel spacing of  $5\ \mu\text{m}$ , while our experiments have a channel spacing of  $\approx 70\ \mu\text{m}$ . A large microtubule vortex forms with a boundary that is  $90\ \mu\text{m}$  in diameter [4], however, our boundaries are  $18\ \text{mm} \times 3\ \text{mm}$ . Further, our experiments use GMPCPP stabilized microtubules with an average length of  $7\ \mu\text{m}$ , while the work reporting vortices uses taxol stabilized filaments with a length range of  $\approx 10\text{-}100\ \mu\text{m}$ . There may also be a significant difference between the acrylamide surface chemistry we

use and the agarose chemistry used in the other work.

### **Extensile vs. Contractile**

We note that our experimental system results in a contractile network rather than an extensile gel. Recent works have shown that conditions leading to a contractile system require long flexible filaments that are capable of buckling and that undergo limited steric interactions [16, 19]. In contrast, the extensile active gel or the active nematic relies on high concentrations of depletion agents to preform bundles of short and stiff filaments, unlike in our system. This suggests that the lack of extensile behavior we observe is unrelated to the optically-dimerizable motors, but rather to the parameters of the microtubule length and depletion agent. Therefore, there is no inherent limitation in the application of optically-dimerizable motors under extensile conditions.

### **2.2.3 Microscopy Protocol**

Samples were imaged at 10X (Fig 1c, 1e, 1f, 2d, 4a, 4f, and 4h) or 20X (Fig. 1d, 2b, 3b, 3d, and 3e). For Figures 2e and 2f, the distance span of the merger experiments required us to pool data taken at 10X (500  $\mu\text{m}$  and 1000  $\mu\text{m}$  separations) and 20X (175  $\mu\text{m}$ , 250  $\mu\text{m}$ , and 350  $\mu\text{m}$  separations) magnifications. For the formation, merging, and movement experiments represented in Figures 1-3, the images of the fluorescent microtubules were acquired every 20 s. For each time point, a z-stack of 5 slices spaced by 10-15  $\mu\text{m}$  is taken. For the flow experiments represented in Figure 4, a brightfield image and subsequent fluorescent image were acquired every 4 seconds to observe the tracer particles and microtubules, respectively, without z-stack imaging. The increased frame rate was needed to ensure sufficient accuracy of the particle velocimetry. For all experiments, we activated light-induced dimerization in the sample every 20 s with a brief 300 msec flash of 2.4  $\text{mW}/\text{mm}^2$  activation light from a  $\approx 470$  nm LED. The rate of activation was based on the estimated off-rate of the iLID-micro complex [14] of  $\approx 30$  s. The duration of the activation light was empirically determined by gradually increasing the time in 50 msec increments until we observed the formation of an aster. We note that higher frequencies of activation or longer pulse duration result in contractile activity outside of the light pattern. Typically, one experiment was run per sample. Individual samples were imaged for up to 1 hour. We placed the time limitations on the sample viewing to minimize effects related to cumulative photobleaching, ATP depletion, and global activity of the light-dimerizable proteins. After several hours, inactivated "dark" regions of the

sample begin to show bundling of microtubules.

#### 2.2.4 Measuring Aster Spatial Distribution with Image Standard Deviation

We interpret the pixel intensity from the images as a measure of the microtubule density. Image standard deviation  $\sigma$  is a measure of the width of an intensity-weighted spatial distribution over a region of interest, ROI. We use  $\sigma$  to characterize how the spatial distribution of microtubules evolves in time. For each time point, we first normalize each pixel value  $I(x, y)$  by the total pixel intensity summed across the ROI,

$$I_{\text{norm}}(x, y) = \frac{I(x, y)}{\sum_{x, y \in \text{ROI}} I(x, y)} \quad (2.1)$$

where  $I(x, y)$  is the raw intensity of the pixel at position  $(x, y)$  after background subtraction. To find  $\sigma$ , we define the image variance  $\sigma^2$  of the intensity-weighted spatial distribution as

$$\sigma^2 = \sum_{x, y \in \text{ROI}} [(x - \bar{x})^2 + (y - \bar{y})^2] I_{\text{norm}}(x, y), \quad (2.2)$$

where coordinates  $\bar{x}$  and  $\bar{y}$  are the center of the intensity distribution

$$\bar{\mathbf{x}} = \sum_{\mathbf{x} \in \text{ROI}} \mathbf{x} I(\mathbf{x}). \quad (2.3)$$

#### 2.2.5 Characteristic Size of an Aster

##### Determining Characteristic Size

As seen in Fig. 2.2, the irregularity of aster arm spacings and lengths presents very challenging segmentation issues for the detailed modeling of the microtubule distribution. Instead, we chose to determine a single characteristic size to represent the spatial distribution of the aster. First, we perform a maximum projection over the z-stack for each time point to create a 2D image in the XY plane. To represent the projected 2D image, we chose the image standard deviation approach (Section 2.2.4) to integrate over the variations in the XY plane. We define the characteristic aster size as the image standard deviation  $\sigma$  after  $\approx 15$  min of activation. The characteristic size is used for comparing with order-of-magnitude scaling arguments (Section 2.2.12).

## 2.2.6 Image Analysis of Asters

### Image Preparation

At each time point, each z-stack of images is summed into a single image in the XY plane. We process each XY image to correct for the non-uniformity in the illumination and background intensity. We “flatten” the non-uniformity of the image with an image intensity profile found in the following process. We take the first frame of the experiment and perform a morphological opening operation with an 80-pixel disk followed by a Gaussian smoothing with a 20-pixel standard deviation. The resulting image is then normalized to its maximum pixel intensity to generate the image intensity profile. Images are flattened by dividing them by the intensity profile. We note that this strategy depends on there being a uniform density of microtubules in the first frame.

Once images are flattened, the background is found by taking the last frame of aster formation and calculating the mean intensity of the activated region that is devoid of microtubules. Images are subtracted by this background intensity and thresholded so that any negative values are set to zero.

### Defining the Regions of Interest

As mentioned in Section 2.2.4, we determine the image standard deviation over a region of interest (ROI). For the formation experiments, we define the region of activation as the disk encompassing the aster and the region devoid of microtubules around the aster, after  $\approx 15$  min of activation, when formation is complete. To identify this region, we segment the low intensity region around the aster. The low intensity region around the aster is found by subtracting the final frame of aster formation from the first frame of the image acquisition. After subtraction, the void region is the brightest component of the image. We segment this region by performing an intensity and size threshold to create a mask. The aster-shaped hole in the mask is then filled. Using the perimeter of the mask, we calculate the diameter of the disk region of activation.

For analyzing the images for the decay process, we alternatively take a region of interest centered on the aster position (from the last frame of aster formation and found using the intensity weighted center) and proportional to the size of the aster in order to reduce the contribution of microtubules diffusing in from the boundary. This proportionality constant was chosen as the ratio of the ROI diameter to the aster diameter for the aster formed with the 50  $\mu\text{m}$  disk, which is 1.63.

### 2.2.7 Reversibility of Aster Formation and Decay

To show that aster decay is driven by motors reverting to monomers as opposed to irreversible events such as ATP depletion or protein denaturation, we provide an illustrative experiment of aster formation followed by decay followed again by aster formation. Imaging for this experiment was performed at 20X to increase the spatial resolution. We note that asters do not completely decay, as observed in panel 6 of Fig. 2.4 that the central core of the aster persists.

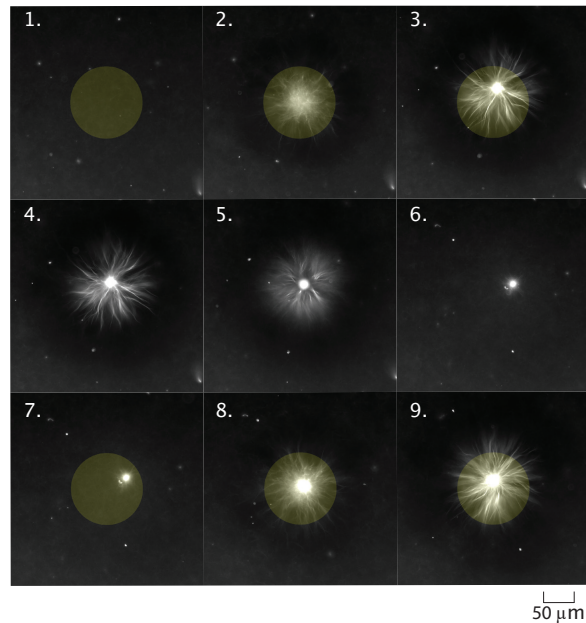


Figure 2.4: Time series of light induced aster formation, decay, then formation. First formation frames are at time points  $t = (1) 0, (2) 6.7, \text{ and } (3) 16.3$  min. Aster decay frames are for  $t = (4) 16.7, (5) 25, \text{ and } (6) 112.7$  min. Second aster assembly frames are  $t = (7) 113, (8) 120, \text{ and } (9) 129.3$  min.

### 2.2.8 Speed and Characteristic Time Scales of Formation and Merging

In order to compare the boundary dependence of our contraction behavior to other contractile networks, we calculate the max speeds and characteristic times of contraction and aster merger as described in [15–17]. We first find the characteristic time by fitting a model to our experimental data and then use this value to calculate the maximum speed. As in [15], we fit to a model of a critically damped harmonic oscillator,

$$L(t) = L_{\text{fin}} + (L_{\text{init}} - L_{\text{fin}}) \left(1 + \frac{t}{\tau}\right) e^{-\frac{t}{\tau}}, \quad (2.4)$$

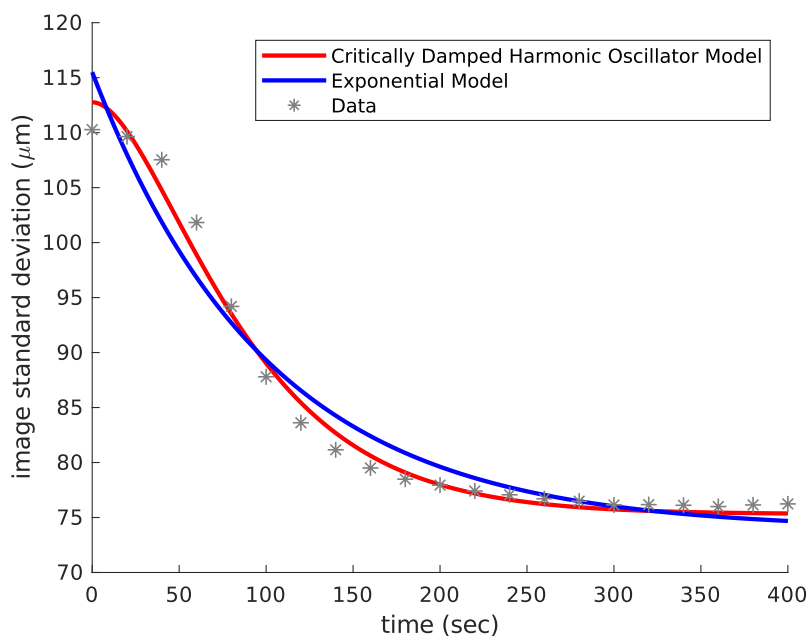


Figure 2.5: A comparison of model fittings for a contracting aster experiment.

where  $L_{\text{init}}$  is the initial size of the network,  $L_{\text{fin}}$  is the final network size, and  $\tau$  is the characteristic time of contraction. This model was developed to describe a contractile actomyosin gel, which shares similar dynamics with our own system. We apply this fit on time points after the initial lag phase, which was empirically determined to end at one minute. While we tried fitting to an exponential function, we found that the harmonic oscillator model was more robust across excitation length scales (Fig. 2.5).

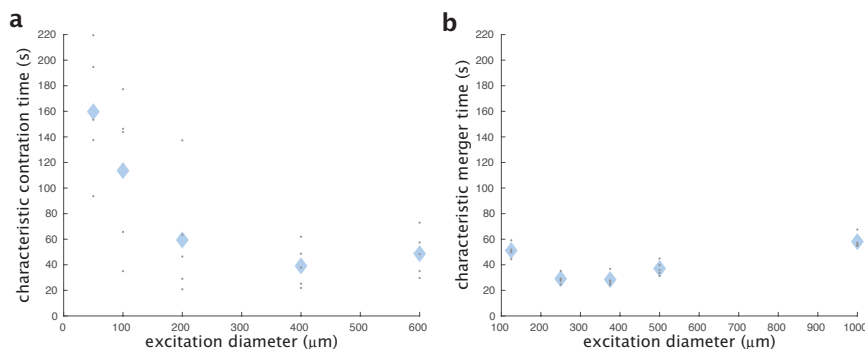


Figure 2.6: Characteristic times for contraction and merger as functions of activation length scales. **a**, Characteristic time for aster formation as a function of the excitation diameter. **b**, Characteristic time for aster merging as a function of the initial distance between asters.

We find that the characteristic times show a general lack of sensitivity to system size for our range of lengths (Fig. 2.6), similar to [17]. The characteristic time is roughly 1 to 2 minutes, comparable to the times reported in [17].

We calculate the maximum speed of contraction or merger,  $v_{\max} = -\frac{dL(t_{\max})}{dt}$ , by finding the time  $t = t_{\max}$  that satisfies  $\frac{d^2L(t_{\max})}{dt^2} = 0$ . First we calculate the second derivative of Eq. 2.4,

$$\frac{d^2L(t)}{dt^2} = \frac{(L_{\text{init}} - L_{\text{fin}})(t - \tau)}{\tau^3} e^{-\frac{t}{\tau}}. \quad (2.5)$$

Based on this equation, it is apparent that the maximum speed occurs at  $t_{\max} = \tau$ . The maximum speed is then defined as  $v_{\max} = -\frac{dL(\tau)}{dt}$ . We calculate  $-\frac{dL(t)}{dt}$  by taking the first derivative of Eq. 2.4,

$$\frac{dL(t)}{dt} = \frac{t(L_{\text{init}} - L_{\text{fin}})}{\tau^2} e^{-\frac{t}{\tau}}, \quad (2.6)$$

then set  $t = \tau$  to find the maximum speed,

$$v_{\max} = \frac{dL(\tau)}{dt} = \frac{L_{\text{init}} - L_{\text{fin}}}{e\tau}. \quad (2.7)$$

This  $v_{\max}$  is the reported contraction or merger speed.

## 2.2.9 Comparison to Light Activated Actomyosin Networks

A system that shows some similar behavior to ours is the light activated actomyosin network in [15]. Here, we note the similarities and differences between the two systems. In the actomyosin network, the actin filaments are globally and permanently crosslinked by the myosin motors in both the dark and the light. In the light, motors are permanently activated. Light patterns generate a localized contraction of the global actomyosin network. Since the contracting region is still linked to the rest of the actomyosin network, deformations are propagated throughout the entire network.

In contrast, our system starts with unlinked microtubule filaments. Light patterns activate linkages of motors to create a localized contractile network with a free boundary. Thus, there are no connections to an external network, unlike the actomyosin system. Further, the reversibility of these links allows the networks to remodel and to resolve after contraction.

A key similarity between the two systems is the observation that contraction speed increases linearly with the size of the excitation region. A recent theoretical treatment [16] provides a generic model for this observation. Their results in Box 1 Panel C predict a linear scaling of contraction speed versus size for 1D, 2D, and 3D networks. For a 1D network, the contraction speed  $\frac{dL}{dt}$  is related to the length  $L$  of the network by the contractility constant  $\chi$  as

$$\frac{dL}{dt} \approx \chi L. \quad (2.8)$$

### 2.2.10 Analysis of Aster Decay

When the activation light is removed, the iLID-micro dimer begins to disassociate, leading to un-crosslinked microtubules. The original work where iLID is designed and characterized shows that the formation and reversion half-lives of individual iLID-micro heterodimers are on the order of 30 seconds [14]. Our empirical determination that sharp localization of contractile forces within the light pattern requires pulsing the light pattern every 20 seconds (Section 2.2.3), in addition to the characterization of other iLID and LOV domain based systems [20–23], supports the notion that the reversion rate of kinesin-fused iLID proteins is similarly on the tens of seconds time scale. We note that the motor density has been predicted and observed to increase exponentially towards the aster center [10]. We therefore expect the central region of the aster to decay more slowly than an individual motor link. This may explain why asters appear to decay on the order of tens of minutes (Fig. 1c), rather than tens of seconds.

For an ideal 2D Gaussian spatial distribution of diffusing particles starting with a finite radius of  $w$ , we expect

$$p(r, t) = \frac{1}{\pi(4Dt + w^2)} e^{-r^2/(4Dt + w^2)}, \quad (2.9)$$

where  $D$  is the diffusion coefficient.

The variance  $\sigma_{\text{Gauss}}^2$  of this distribution as a function of time  $t$  is given by

$$\sigma_{\text{Gauss}}^2(t) = 4Dt + w^2. \quad (2.10)$$

The variance  $\sigma_{\text{Gauss}}^2$  increases linearly with  $t$  with a slope of  $4D$ .

We characterize the aster decay process by measuring the image variance  $\sigma^2$  as a function of time, as described in (SI. 2.2.4). Images are first processed as described

in (SI. 2.2.6). Although our spatial distributions are not strictly Gaussian, we observe that for our data  $\sigma^2$  increases linearly with  $t$  (Fig. 2.7), which suggests that the decay process is described by the diffusion of unbound microtubules. By analogy to the 2D ideal Gaussian case, we calculate an effective diffusion coefficient of our distributions by a linear fit of  $\sigma^2$  versus time and find the diffusion coefficient from the slope. This gives us a diffusion coefficient in units of  $\mu\text{m}^2/\text{s}$ .

We find the diffusion coefficient by applying a linear fit to time points that occur after 200 seconds.

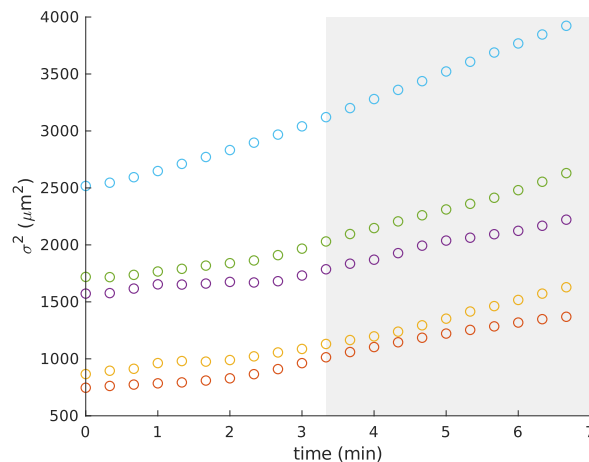


Figure 2.7: Plot of mean variance of image intensity as a function of time for different initial aster sizes. The shaded region is treated as part of the linear regime. The measure of time is relative to the beginning of aster decay.

### 2.2.11 Diffusion Coefficient of a Microtubule

We approximate the diffusion coefficient for a single microtubule as a rigid rod to compare with the effective diffusion coefficient we estimate for aster decay. The diffusion coefficient  $D$  for an object in liquid media can be calculated from the drag coefficient  $\gamma$

$$D = \frac{k_B T}{\gamma}, \quad (2.11)$$

where  $k_B$  is the Boltzmann constant and  $T$  is the temperature, for which we use 298 K. We model a microtubule as a  $7 \mu\text{m}$  long cylinder (SI. 2.7.2) with a radius of 12.5 nm. The drag coefficients for a cylinder have been found previously [24] for motion

either parallel  $\gamma_{\parallel}$  or perpendicular  $\gamma_{\perp}$  to the long axis of the cylinder

$$\begin{aligned}\gamma_{\parallel} &= \frac{2\pi\eta L}{\ln(L/2r) - 0.20}, \\ \gamma_{\perp} &= \frac{4\pi\eta L}{\ln(L/2r) + 0.84}.\end{aligned}\tag{2.12}$$

Here,  $L$  is the length of the cylinder,  $r$  is its radius, and  $\eta$  is the viscosity of the fluid, which we estimate to be  $2 \times 10^{-3}$  Pa  $\cdot$  s (SI 2.5.8). Using the parameters detailed above, we calculate  $D_{\parallel} = 0.3 \mu\text{m}^2/\text{s}$  and  $D_{\perp} = 0.2 \mu\text{m}^2/\text{s}$ . We assume that the larger diffusion coefficient dominates and thus use  $D_{\parallel}$ , the longitudinal diffusion coefficient, as the diffusion coefficient for a single microtubule in Fig. 1e.

### 2.2.12 Scaling Arguments for Aster Size and Comparison to Data

We consider how the total number of microtubules in an aster relates to the volume of the projected light pattern. We are projecting a disk pattern of light on the sample from below. The channel is a constant height,  $z \approx 70 \mu\text{m}$ . We therefore treat the light excitation volume as a cylinder  $V_{\text{light}} = \frac{1}{4}\pi z d_{\text{light}}^2$  where  $d_{\text{light}}$  is the diameter of the excitation disk. If we look at experimental data, we see evidence of a linear relationship between the light volume and the number of microtubules that are present during aster formation (Fig. 2.8a). The implication of this observation is that the density  $\rho$  of microtubules is uniform. Furthermore, we see that after the initial contraction event, the total integrated fluorescence of the excited region remains constant (Fig. 2.8b), indicating that the total number of microtubules  $N$  is constant during aster formation.

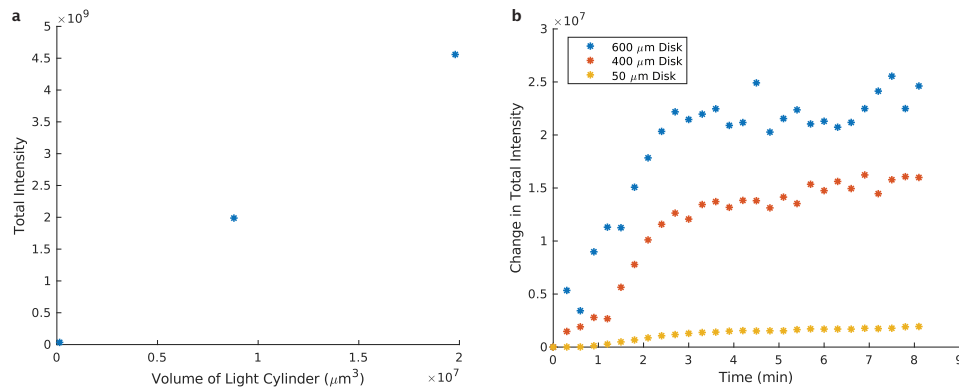


Figure 2.8: Measuring the conservation of labeled fluorescent microtubules in the excitation region during aster formation. **a**, Total intensity of excitation region as a function of volume of light cylinder averaged during aster formation. Measurements are for light disks with diameters 50, 400, and 600  $\mu\text{m}$ . **b**, Change in total intensity inside of the excitation region as a function of time.

Based on these observations, we assume that the number of microtubules  $N$  in the aster is given by

$$N \approx \rho V_{\text{light}}. \quad (2.13)$$

From Section 2.2.1, we observe that asters have a roughly spheroidal symmetry. For an order-of-magnitude estimate of how aster size scales with the volume of light, we assume that the characteristic length of the aster  $L_{\text{aster}}$  is given by the diameter of an effective sphere which scales with microtubule number as

$$L_{\text{aster}} \propto N^{1/3}. \quad (2.14)$$

and thus

$$L_{\text{aster}} \propto V_{\text{light}}^{1/3}. \quad (2.15)$$

As noted above, if the volume defined by the activation light is a cylinder, then

$$V_{\text{light}} \propto d_{\text{disk}}^2. \quad (2.16)$$

From these last two equations, we arrive at the scaling relationship between aster size and excitation disk size

$$L_{\text{aster}} \propto d_{\text{disk}}^{2/3}. \quad (2.17)$$

We made a power law fit with a fixed exponent of  $2/3$  to the data shown in Fig. 1f. Though we cannot strictly rule out other exponents, we show the fit to demonstrate that the scaling argument determined exponent is at least consistent with the data.

### 2.3 Aster Dynamics

Moving activation patterns are responsible for dynamically re-positioning structures and forces within a cell [25]. We are able to similarly move asters by re-positioning light patterns relative to the sample slide by moving the slide stage (Fig. 2.9a). We are also able to move asters by directly moving the light pattern, however, moving the stage allows for a greater range of travel. As the stage moves, the asters track with the light pattern, traveling up to hundreds of microns relative to the slide (Fig. 2.9b) (Video 4) (Section 2.3.1). The aster maintains a steady state distance  $\ell$  between itself and the light pattern (Fig. 2.9c). We find that asters are always able to track the pattern for stage speeds up to 200 nm/s. At 400 nm/s, asters are not able to stay with the pattern, setting an "escape velocity" that is comparable to the motor speeds measured in gliding assays (Section 2.3.4). When the stage stops moving, the aster returns to the center of the light pattern, indicating that the aster is experiencing a restoring force. We can characterize aster movement as caused by an effective potential (Section 2.3.2), and observe mesoscopic phenomena that may inform the underlying mechanisms of aster motion (Section 2.3.3).

Intriguingly, we find that asters formed near each other interact by spontaneously merging. To study this interaction, we construct an aster merger operation, where asters are connected with light (Fig. 2.9d) (Video 5). At the beginning of the merging process, a network of bundled microtubules forms, which connects the asters. The connecting network begins to contract and the asters move towards each other (Fig. 2.9e). The speed at which asters merge (Section 2.2.8) increases as a function of linking distance up to a speed of roughly 2.5  $\mu\text{m/s}$  (Fig. 2.9f). The scaling of aster merger speed as a function of distance is similar to the observed relationship of contraction speed as a function of the excitation cylinder size discussed above. We note that the maximum observed merger speed is about an order of magnitude higher than the speeds observed during gliding assays (Section 2.3.4), which is analogous to how cell migration speeds can exceed single motor speeds [26]. Our ability to move and merge microtubule asters reveals that they are not steady state structures as previously observed [5], but are dynamic and constantly remodeling.

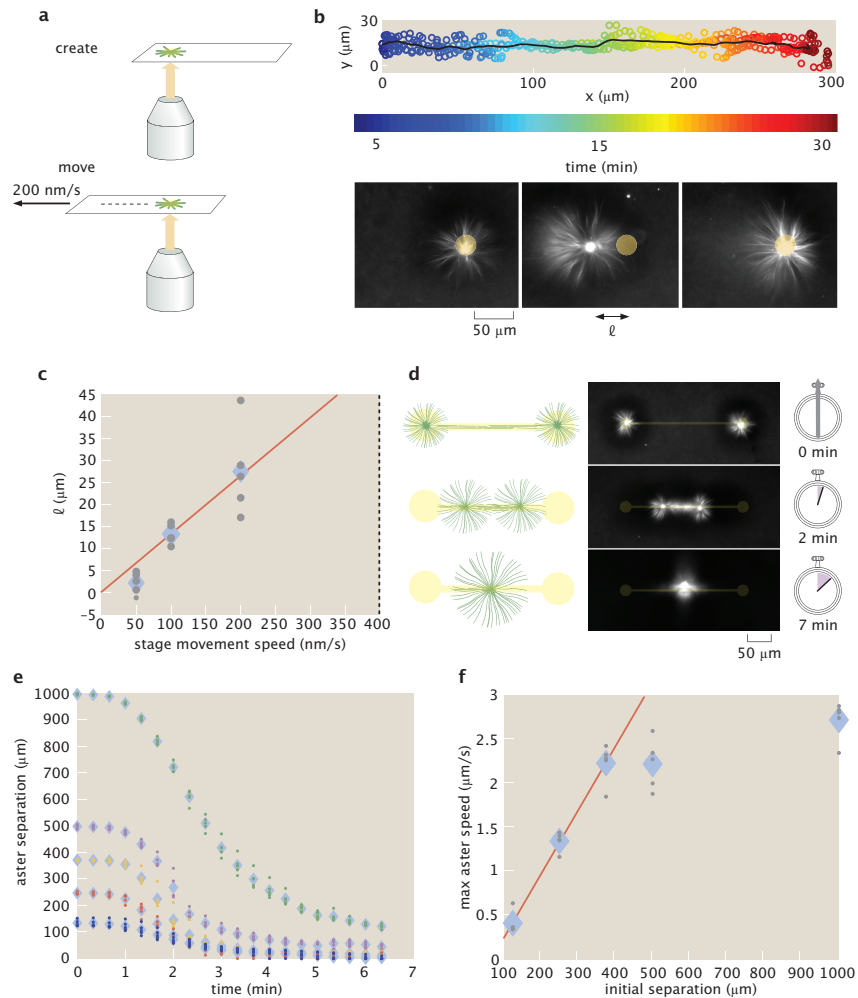


Figure 2.9: Moving and merging operations of asters with dynamic light patterns. **a**, Asters are moved relative to the slide by repositioning the microscope stage. **b**, Overlay of five individual trajectories of aster movement relative to slide moving at 200 nm/s. The line represents the mean trajectory. Time lapse images show the position of the aster relative to the light pattern.  $\ell$  is the displacement of the aster from center of the light pattern. **c**,  $\ell$  versus stage speed. The dotted line at 400 nm/s represents the escape velocity. The red line is a linear fit. **d**, Illustration of the aster merge operation by a connected excitation pattern and the corresponding time series of images. **e**, Distance between merging asters over time for different initial separations. **f**, Maximum speeds of asters as measured from (e). The red line is a linear fit to the first three data points. In (c, e, f), the diamonds represent the mean of 5 experiments and the dots represent individual experiments.

### 2.3.1 Tracking of Moving Aster

For each time point, we sum over the z-stack to form a single image. The image is then passed through a morphological top-hat filter with a structure element of a 100-pixel disk to “flatten” non-uniformities in the illumination. The image is then

projected into a 1D intensity profile. We project onto the x-axis by summing along the line that passes through the center of the excitation disk with a 100-pixel window in y. Aster centers are then found at each frame by fitting the intensity profiles to Gaussian functions.

For 2D tracking, the movement of the aster is found by comparing the centroid of the aster in each frame. The raw images are processed using a Gaussian filter with a standard deviation of 1 pixel, followed by thresholding to eliminate the background noise.

### 2.3.2 Effective Potential of a Moving Aster

When the light pattern moves, we observe that the aster appears to be pulled in tow behind the light pattern, perhaps by the aster arms or newly-formed microtubule bundles in the light pattern. Further, when the light pattern stops moving at speed  $v_{\text{light}}$ , we observe that the aster immediately returns to the center of the light pattern at speed  $v_{\text{return}}$ . From Fig. 2.10, we see that

$$v_{\text{return}} \approx v_{\text{light}}. \quad (2.18)$$

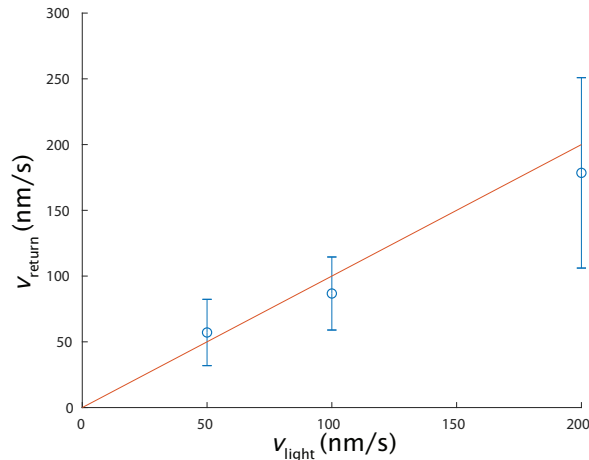


Figure 2.10: The speed at which an aster returns to the center of the light pattern once the pattern stops moving. Red line is a plot of  $y = x$ .

This is the behavior expected for an object under the influence of a potential at low-Reynolds-number, where the aster has negligible momentum and the forces are essentially instantaneous. These observations support the notion that a moving aster can be modeled as being in an effective potential. First, we model the observed behavior with a generic potential without any assumption of the mechanistic cause

of the potential and then numerically compare these results to the estimated optical tweezer effects of the excitation light pattern.

We estimate the potential and the forces acting on a moving aster from the viscous drag of the background fluid, in an analogous way to how this is done for objects trapped in an optical tweezer [27]. If we assume that the aster is a spherical object of radius  $a$  and is moving with speed  $v_{\text{light}}$ , it will experience a viscous drag force  $F_{\text{drag}}$  :

$$F_{\text{drag}} = 6\pi\eta av_{\text{light}}, \quad (2.19)$$

where  $\eta$  is the fluid viscosity.  $F_{\text{drag}}$  is equal to the force  $F_{\text{pull}}$  that is pulling the aster towards the light pattern. From the results of Fig. 2c, we note that the observed distance shift  $\ell$  of the aster from the center of the moving light pattern is roughly linear with excitation disk movement speed  $v_{\text{light}}$ . The linearity of  $\ell$  versus  $v_{\text{light}}$  implies that  $F_{\text{pull}}$  acts like a spring:

$$F_{\text{pull}} \approx k_{\text{spring}}\ell, \quad (2.20)$$

where  $k_{\text{spring}}$  is the spring constant. Setting these two forces equal gives a spring constant of

$$k_{\text{spring}} \approx \frac{6\pi\eta av_{\text{light}}}{\ell}. \quad (2.21)$$

The effective potential  $U_{\text{pull}}$  for this force is

$$U_{\text{pull}} = \frac{1}{2}k_{\text{spring}}\ell^2. \quad (2.22)$$

The aster in Fig. 2c is  $\approx 25 \mu\text{m}$  in diameter. Assuming that  $\eta \approx 2 \times 10^{-3} \text{ Pa} \cdot \text{s}$  (SI 2.5.8), we find that  $k_{\text{spring}} \approx 3 \times 10^{-15} \text{ N}/\mu\text{m}$ . For the maximum observed displacement of  $\ell \approx 30 \mu\text{m}$ , the energy stored in the potential, or equivalently, the work done by the system to return the aster back to the center of the light pattern is  $\approx 300 k_B T$ .

The spring constant of an optical tweezer trapping polystyrene spheres is  $\approx 1 \times 10^{-9} \text{ N}/\mu\text{m}$  for a  $\approx 1000 \text{ mW}$  laser beam focused to  $\approx 1 \mu\text{m}$  diameter [28]. Accounting for light intensity, we estimate the spring constant to be  $\approx 1 \times 10^{-12} \text{ N}/\mu\text{m}$  per  $\text{mW}/\mu\text{m}^2$ . In comparison, our light pattern has an intensity of  $2.4 \text{ mW}/\text{cm}^2$ . The light is on only for 0.3 sec every 20 sec (SI 2.2.3), giving a time averaged intensity of  $0.036 \text{ mW}/\text{cm}^2$ . The estimated upper bound spring constant from the light pattern due to optical tweezing effects is  $\approx 3.6 \times 10^{-22} \text{ N}/\mu\text{m}$ , roughly a factor of  $10^7$  weaker than

the spring constant we observe. Further, we note that it is a generous assumption that a microtubule aster is refractile as a polystyrene sphere. Given the unlikelihood of optical tweezing being related to the potential we observe, we attribute the effective potential other effects such as the remodeling of the microtubule field.

### 2.3.3 Mechanism and Stability of a Moving Aster

While the molecular details of aster movement remains a topic of future study, there are mesoscopic phenomena that we observe. When the light pattern activates a region adjacent to the aster, microtubule bundles form. As the light pattern moves, a stream of bundles spans from the light pattern towards the aster. This behavior can be most clearly seen at the highest stage speeds of 200 nm/s and with larger disk sizes (Fig. 2.11).

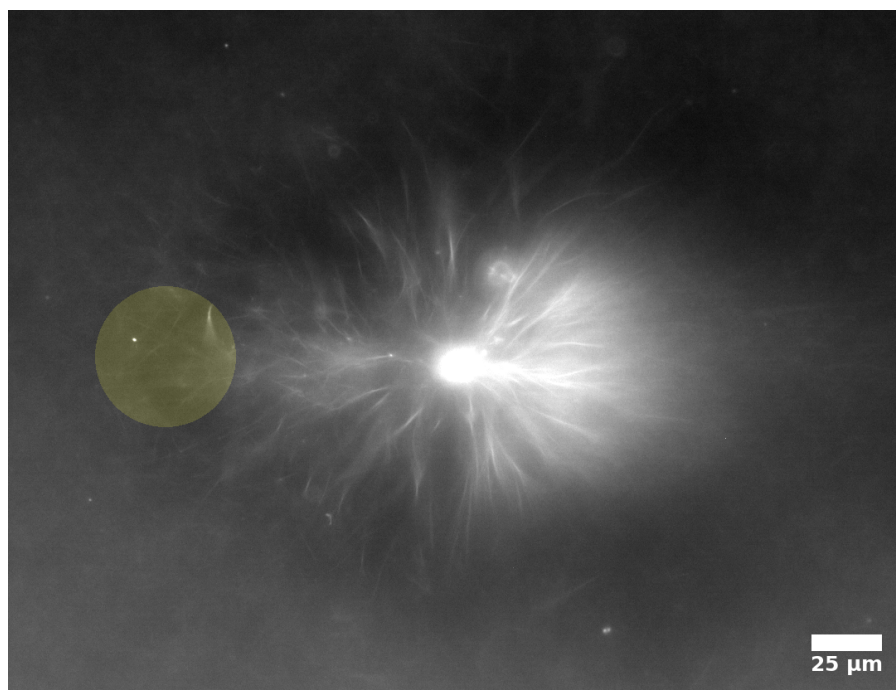


Figure 2.11: Aster following a 50  $\mu\text{m}$  disk moving at 200 nm/s from right to left. Image is integrated across  $z$ .

The stream of bundles appears to pull against the arms of the aster towards a new contractile center.

During aster movement, we observe that a cloud of unbundled microtubules are left in the wake of a moving aster, indicating that there is a decay process occurring. At the same time, however, we also observe that microtubules are incorporated into the aster, as demonstrated by the increase in the aster intensity over time (Fig. 2.12),

which starts to occur after a few minutes. The increase in intensity also indicates that the incorporation rate is greater than the aster decay rate. We speculate that the newly added microtubules deliver linked motor proteins that maintain some of the bonds between filaments, allowing the aster to persist outside of the light pattern.

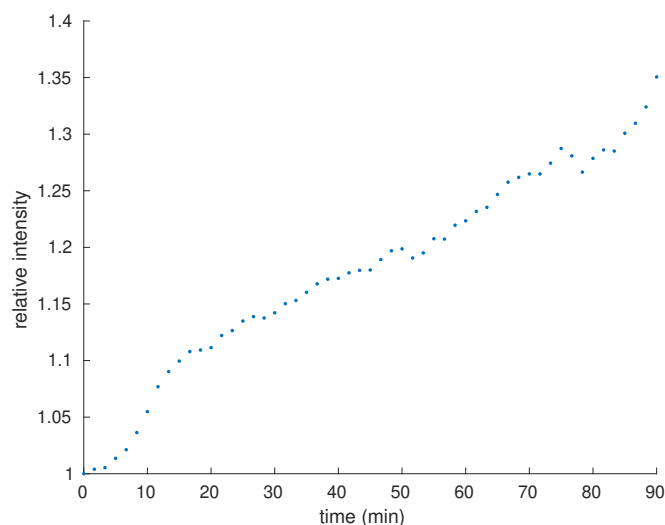


Figure 2.12: Intensity of an aster for a light pattern moving at 200 nm/s. The y-value is normalized to the intensity at  $t = 0$ . Intensity is measured for an ROI with a fixed diameter and tracks with the aster center.

### 2.3.4 Single Motor Velocity Determination from Gliding Assay

Gliding assay images were acquired every second with total internal reflection fluorescence (TIRF) microscopy. Motor speeds were determined by tracking individual microtubules. Single microtubules were identified by edge detection followed by size thresholding to remove small particles on the glass and large objects that are overlaying microtubules. The centroid of each object is identified and paired with the nearest-neighbor in the next frame. The Euclidian distance between the paired centroids is calculated and used to determine the microtubule velocity. The mean motor speed was determined from the mean frame-by-frame velocities (excluding those less than 75 nm/s, which is our typical sample drift).

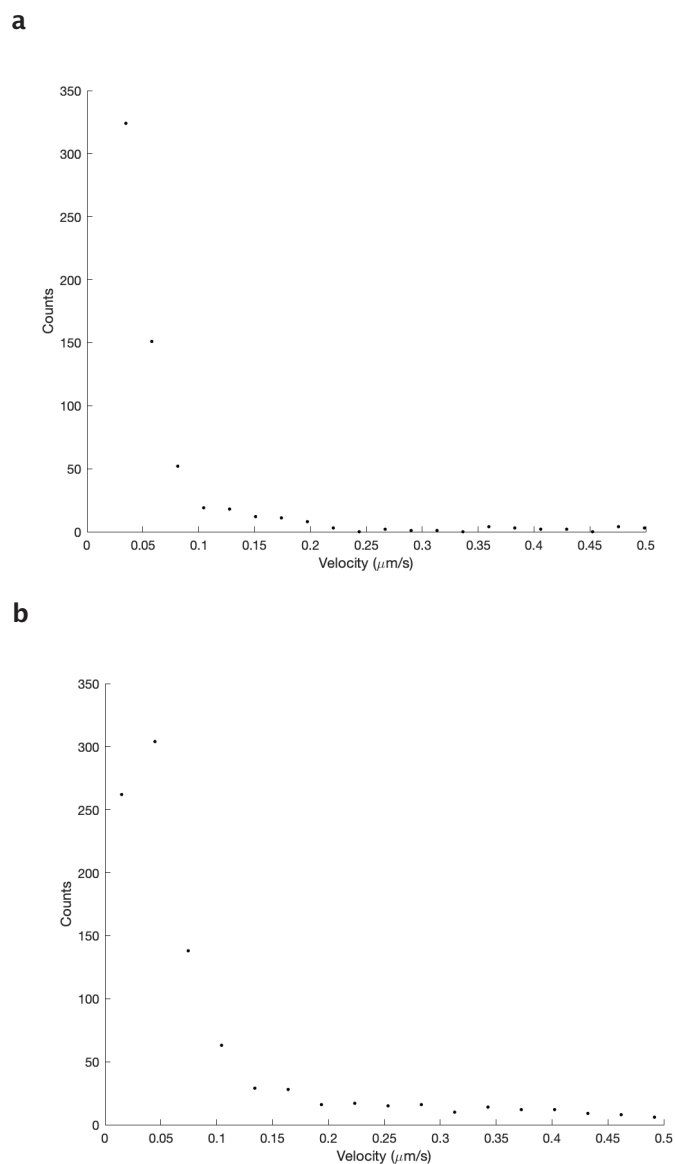


Figure 2.13: Velocity distribution of gliding microtubules. **a**, Binned velocities for K401-iLID motors; the mean of the data is 230 nm/s with a standard deviation of 200 nm/s. **b**, Binned velocities for K401-micro motors; the mean of the data is 300 nm/s with a standard deviation of 250 nm/s.

## 2.4 Programming Aster Patterning and Trajectories with Light

The capability to perform successive operations remains a fundamental step towards engineering with active matter. Our ability to form dynamic light-defined compartments of active molecules enables us to execute multiple aster operations. By composing aster creation operations, we are able to form asters of differing sizes and place them at prescribed positions in parallel (Fig. 2.14a, b) (Video 6). Once

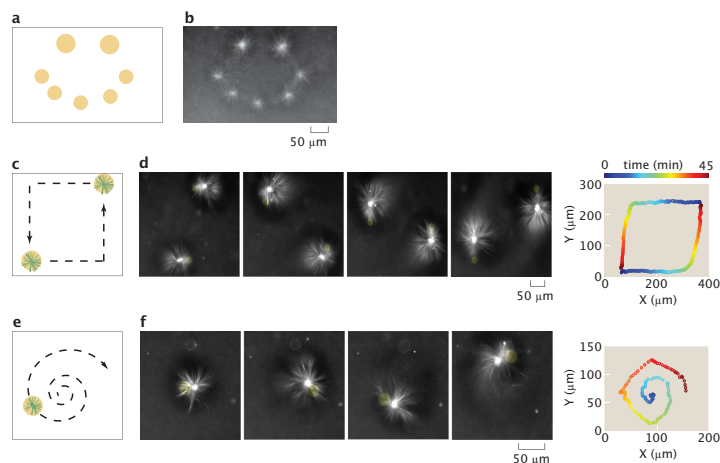


Figure 2.14: Operations for creating and moving asters are composed to make different desired patterns and trajectories. **a**, Sketch for using excitation cylinders to simultaneously pattern asters of different sizes. **b**, Resultant pattern of asters corresponding to (a). **c**, Illustration of simultaneous control of two different aster trajectories, as indicated by the dashed arrows. **d**, Time lapse and the 2D trace of the aster trajectories corresponding to (c). The trajectory trace is color-coded to represent progression in time. **e**, Dynamically projected spiral to illustrate curvilinear motion. **f**, Time lapse and the 2D trace of the aster trajectory. Time is color-coded as in (d).

asters are created, they can be simultaneously moved by using multiple dynamic light patterns (Fig. 2.14c, d) (Video 7). Further, aster trajectories are not limited to rectilinear motion, but can be moved along complex trajectories (Fig. 2.14e, f) (Video 8). During movement, there are inflows of microtubule bundles created in the light pattern, which feed into the aster. There are also outflows of microtubules, which appear as comet-tail streams following the asters (Fig. 2.14d, f). These mass flows illustrate some of the complex non-equilibrium dynamics that are introduced by moving boundaries of molecular activity. The new capability to simultaneously generate and manipulate asters provides a basis for “programming” complex systems of interacting non-equilibrium structures.

## 2.5 Controlling Advective Fluid Flow With Active Matter

In our aster merging, moving, and trajectory experiments, we observe that the fluid flow of the buffer, as inferred by the advection of microtubules and small fluorescent aggregates. Similar cytoskeletal-driven flow is critical for the development and morphogenesis of various unicellular and multicellular organisms [29–35].

Based on these observations, we seek to generate and tune flows in our engineered

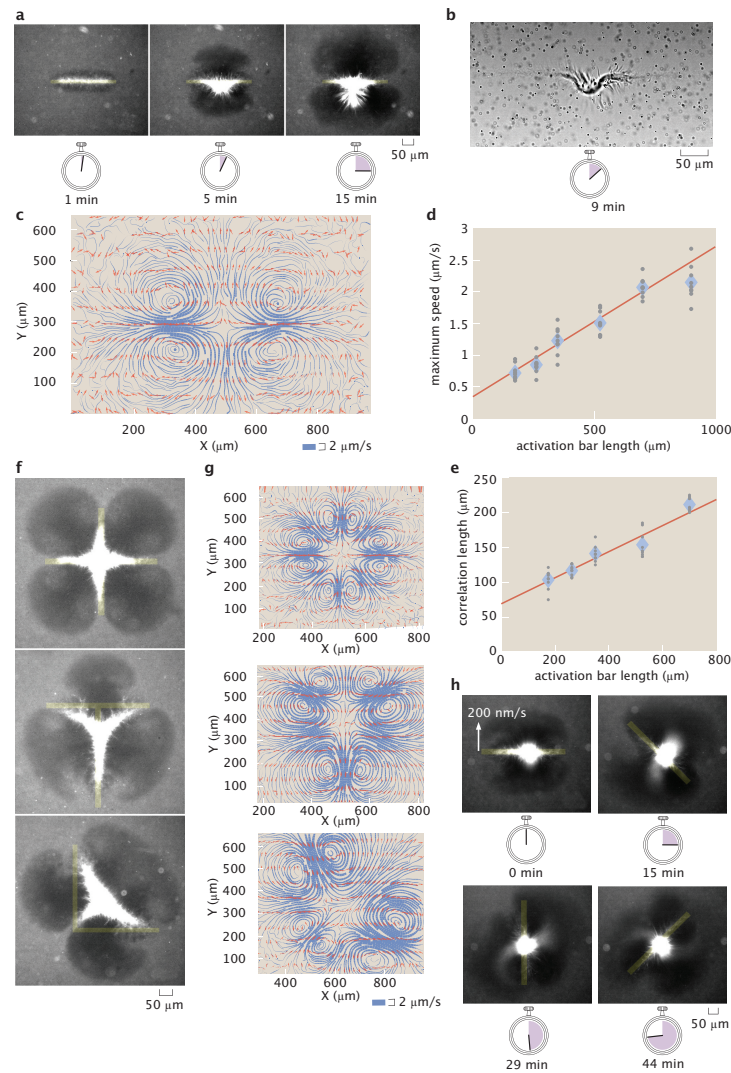


Figure 2.15: Advective fluid flow is created and controlled with patterned light. **a**, Microtubule organization created by an activation bar that is a  $350\ \mu\text{m} \times 20\ \mu\text{m}$  rectangular light pattern. Time series demonstrate continuous contraction of microtubules towards the pattern center along the major axis. **b**, Brightfield image of **(a)** shows a contracting microtubule network and tracer particles used to measure fluid flow. **c**, Streamline plots of background buffer flow from **(a)**. The streamline thickness represents the flow speed. The arrows indicate the flow direction. **d**, Averaged maximum flow speed versus activation bar length. **e**, Averaged correlation length (size) of flow field versus activation bar length. **f**, Superposition of activation bars generate different patterns of contractile microtubules. **g**, Corresponding streamline plots. **h**, Time lapse of a light pattern rotating with an edge speed of  $200\ \text{nm/s}$ . In **(d)**, **(e)**, the diamonds represents the mean of 9 experiments and the gray dots represent individual experiments. The red line is a linear fit to the data.

system with light, which may also provide insight into the mechanics of cellular fluid flow. Recent work has used light to thermally induce cytoplasmic flows [36]. Here, we can generate fluid flows with light by activating contractile microtubule networks with the rectangular bar pattern used during aster merging (Fig. 2.15a) (Video 9). Brightfield images reveal a structurally changing microtubule network (Fig. 2.15b) (Video 10), which appears to drive the fluid flow. We observe there are minimum size and angle limits for these microtubule structures, as well as for asters (Section 2.5.1).

We measure the flow fields with tracer particles (Section 2.5.2). The pattern of the flow is 2D (Section 2.5.3) and stable throughout the experiment (Section 2.5.4), consisting of inflows and outflows of microtubules, as illustrated by streamline plots (Fig. 2.15c)(Section 2.5.5). The competition of these flows ensures that microtubules do not continuously accumulate in the illuminated region and that the surrounding medium is not completely depleted of microtubules.

We manipulate the properties of the flow field through the geometry of the activation volume. The size (Section 2.5.6) and speed of the flow field depend linearly on the length of the activation bar (Fig. 2.15d, e). The scaling of the flow speed is similar to the relationships for both the formation rate versus activation diameter and the aster merging speed versus separation. The positioning and number of inflows, outflows, and vortices are determined by the extrema of the light pattern geometry (Fig. 2.15f, g) (Video 11, Video 12, Video 13). A model that uses a series of point forces following the observed microtubule networks is able to recreate similar inflows and outflows (Section 2.5.7), suggesting that forces from microtubule bundles drive the flow.

Furthermore, the shape of the flow field has a temporal dependence on the light pattern. We modulate the flow field to create an “active stir bar” by applying a rotating light pattern (Fig. 2.15h) (Video 14). While simplified active matter systems are able to spontaneously generate global flows [6, 8], *in vivo* cytoskeletal-driven fluid flows can be controlled and highly structured [29, 30, 34]. Our results demonstrate the creation and dynamic manipulation of localized, structured fluid flow in an engineered active matter system for the first time.

### **2.5.1 Minimum Size Limits of Structures**

Here we explore the minimum feature sizes that we can generate. To test the limits for flow generation, we vary the length and height of the excitation bar. We observe

that the minimum excitation bar length that is able to generate flows is between  $87.5\text{-}175\ \mu\text{m}$  (Fig. 2.16), which corresponds to a microtubule network of  $\approx 100 \times 30\ \mu\text{m}$ . We note that this length is similar to the bundle buckling length observed in Fig. 4b. We speculate that the limits of the minimum length pattern for generating flow may be related to this buckling length scale.

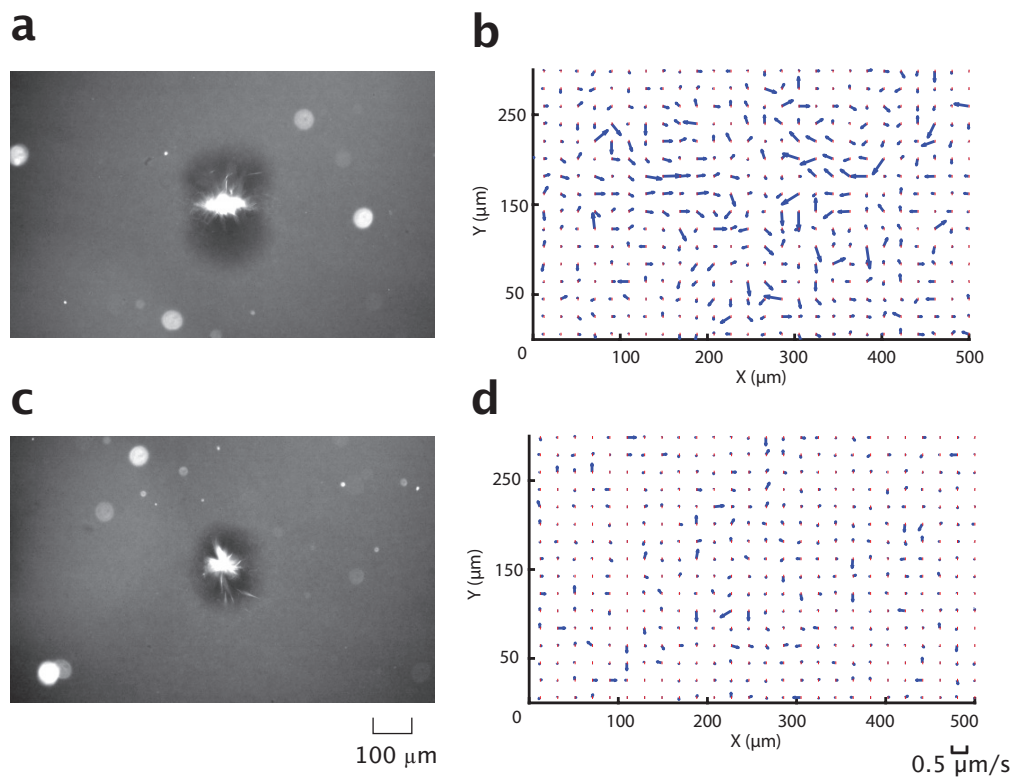


Figure 2.16: Minimum length experiment for a  $L \times 20\ \mu\text{m}$  excitation pattern. **a**, Fluorescent microtubule channel for  $L = 175\ \mu\text{m}$ . **b**, Corresponding flow field to **(a)**. **c**, Fluorescent microtubule channel for  $L = 87.5\ \mu\text{m}$ . **d**, Corresponding flow field to **(c)**.

In addition, we find that the minimum height of an excitation bar that can generate flow is  $\approx 2\ \mu\text{m}$  Fig. 2.17. We observe that the network that forms is  $\approx 300 \times 20\ \mu\text{m}$ . Below this excitation limit, we observe the formation of unstable microtubule bundles that do not persist long enough to form a more ordered structure. While the excitation bar extends  $350\ \mu\text{m}$ , we speculate that below the minimum height, the density of active motors is too low to completely drive organization. This may be a result of the diffusivity and speed of the motor proteins.

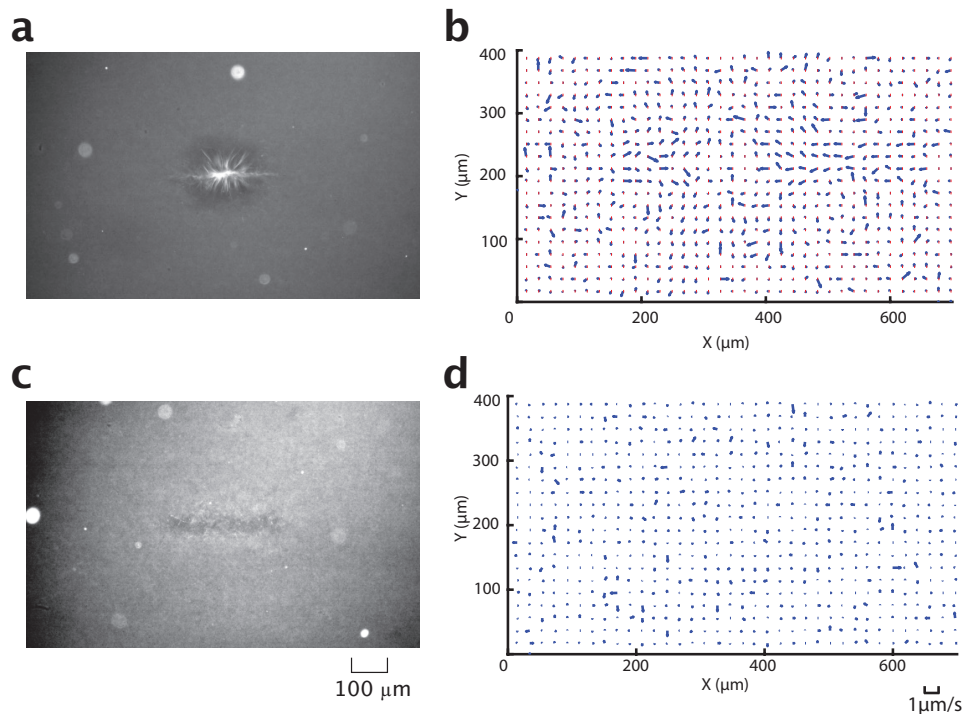


Figure 2.17: Minimum height experiment for a  $350 \times H \mu\text{m}$  excitation pattern. **a**, Fluorescent microtubule channel for  $H = 2 \mu\text{m}$ . **b**, Corresponding flow field to **(a)**. **c**, Fluorescent microtubule channel for  $H = 1 \mu\text{m}$ . **d**, Corresponding flow field to **(c)**.

We determine the angle resolution by taking two overlapping bars, as in the “+” shape shown in Fig. 4f, and rotating them relative to each other. When the bars are orthogonal to each other, there are four distinct inflows at the corners. We decrease the angle between the bars until the flow pattern appears to be that of a single bar (two inflows). The minimum angle between two bar patterns for which there remain 4 distinct inflows and outflows is between  $\frac{\pi}{16} - \frac{\pi}{8}$  (Fig. 2.18). The angle that sets this limit may in part be set by the average length of the filament bundles that form orthogonal to the major axis of each bar pattern, which are  $\approx 20 \mu\text{m}$  in length. For a sufficiently shallow angle, these orthogonal bundles may interact with each other and cause the two microtubule networks to be pulled into each other, merging into a single linear structure. The flow pattern and microtubule distribution of Fig. 2.18c and d closely resemble those produced by a single rectangular bar of light.

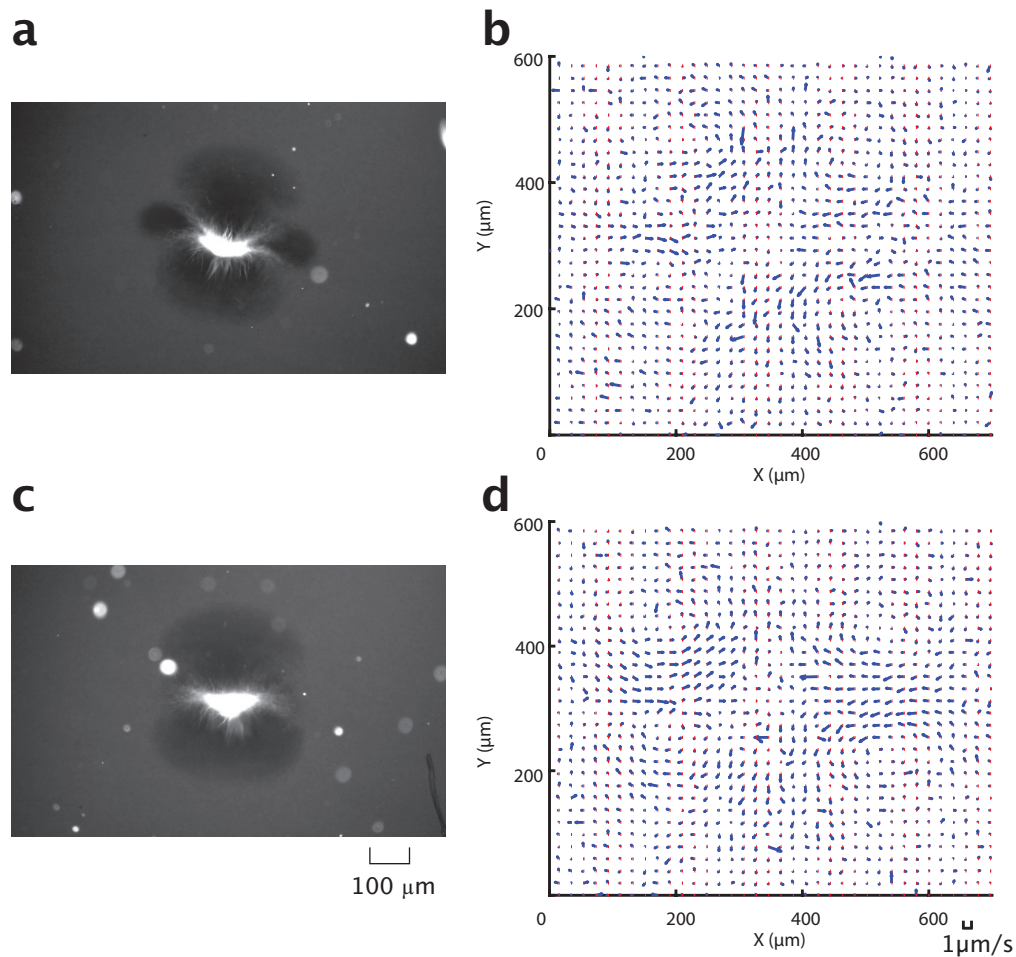


Figure 2.18: Minimum angle experiment for two  $350 \times 20 \mu\text{m}$  excitation pattern. **a**, Fluorescent microtubule channel for an angle of  $\frac{\pi}{8}$ . **b**, Corresponding flow field to **(a)**. **c**, Fluorescent microtubule channel for an angle of  $\frac{\pi}{16}$ . **d**, Corresponding flow field to **(c)**.

We find that the minimum disk diameter to form an aster is between  $6.25 - 12.5 \mu\text{m}$  (Fig. 2.19). The arms of the smallest aster we are able to form appear to be  $\approx 20 \mu\text{m}$ . We note that below this limit, small microtubule bundles form transiently and remain disordered. Due to the similarity of the minimum excitation length scale to the average microtubule length, we hypothesize that the smallest aster we can form may in part be determined by the microtubule length distribution.

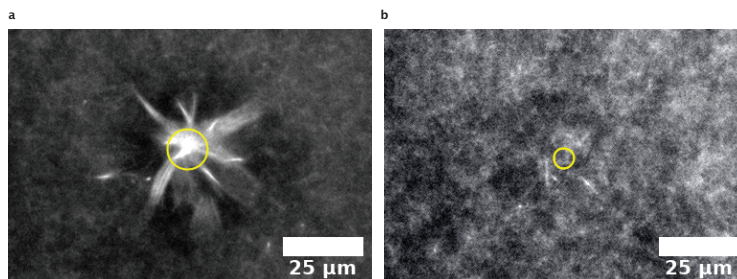


Figure 2.19: Minimum aster size experiment for disk patterns. **a**, Fluorescent microtubule channel for a 12.5  $\mu\text{m}$  excitation disk. **b**, Fluorescent microtubule channel for a 6.25  $\mu\text{m}$  excitation disk. The yellow circle represents the perimeter of the excitation disk.

### 2.5.2 Fluid Flow Patterns from Particle Tracking

The fluid flow generated by the movement of microtubule filaments is measured using Particle Tracking Velocimetry (PTV) [37] of fiducial tracer particles. Inert 1  $\mu\text{m}$  diameter microspheres (SI 2.7.6) are added to the reaction buffer and imaged with brightfield microscopy. The images are pre-processed using a Gaussian filter with a standard deviation of 1 pixel, followed by thresholding to eliminate the background noise. After filtering, the centroid of each particle is measured and tracked.

A nearest-neighbor algorithm [38] is applied to find particle pairs within a square search window (30 pixels). Displacement vectors are then calculated by comparing the position of particle pairs in consecutive frames. The same process is repeated for the entire image sequence (30 min). The velocity field is generated by dividing the displacement vector field by the time interval between frames. The averaged velocity field shown in Fig. 2.20 is carried out by grouping and averaging all velocity vectors within a 30-pixel  $\times$  30-pixel window.

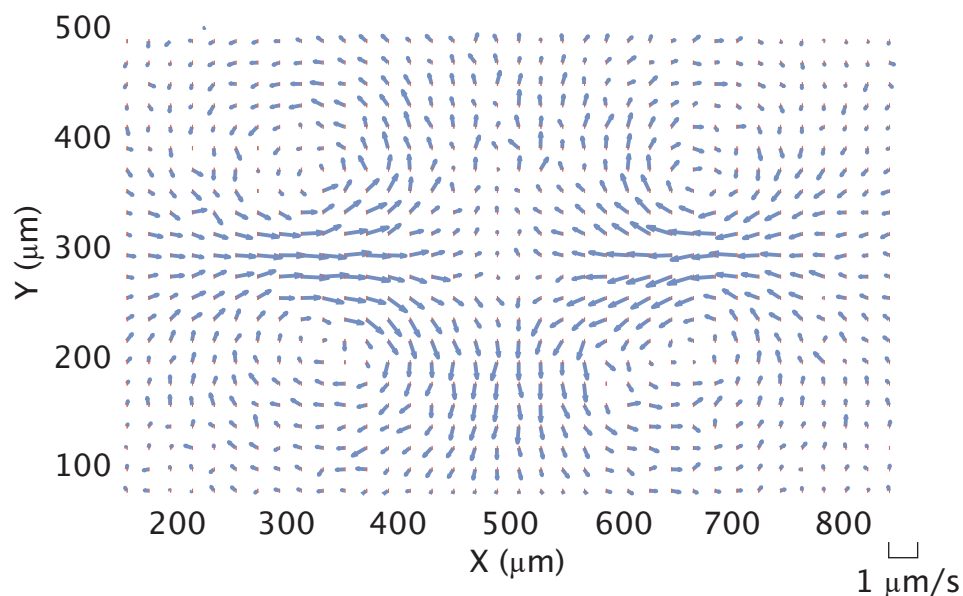


Figure 2.20: Flow velocity field generated with a 350  $\mu\text{m}$  activation bar measured with PTV of tracer particles. Vector data is used to calculate streamline plot in Fig. 4c.

### 2.5.3 2D Flow Field

We measure the flow field at different focal planes to determine its  $z$ -dependence. The flow fields are generated from PTV, as previously described (SI 2.5.2). We image a  $z$ -stack of 3 planes separated by 20  $\mu\text{m}$ , where the sample typically extends  $\approx 70\mu\text{m}$  in the  $z$ -direction. Following the same particle tracking algorithm, we retrieve the flow fields (Fig. 2.21) averaged over a 20 min time window. We do not observe significant differences in the flow field's structure or speed at the various  $z$ -positions. Therefore, for all subsequent flow measurements we image a single focal plane. Further, when we model the flow field (SI 2.5.7), we assume that it is a 2D pattern.

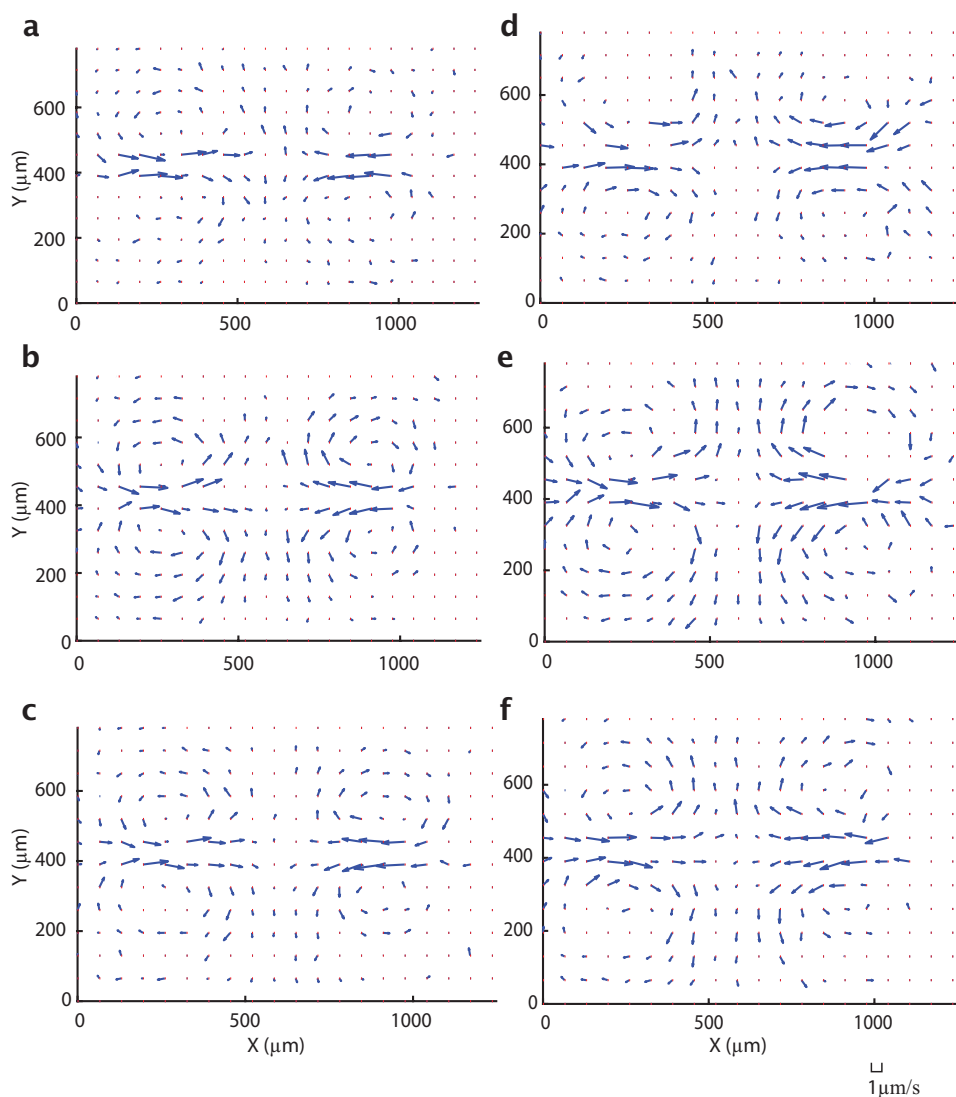


Figure 2.21: A flow field measured at three different z-positions separated by 20  $\mu\text{m}$ . The field is generated with a 700  $\mu\text{m}$  activation bar. **a**, Highest z-position, **b**, middle z-position, **c**, lowest z-position. **d**, **e**, **f**, are from another experiment following the same order.

### 2.5.4 Time Stability of Flow Patterns

In order to understand how the flow field changes in time, we divide the 30-minute experiment into four 7.5-minute time windows and calculate the flow field for each window. The resulting velocity fields are shown in (Fig. 2.22). We note that the structure of the flow field remains similar throughout the experiment. In addition, the maximum speed of the velocity field is constant over time (Fig. 2.23), which further confirms that the fluid flow is stable over the experiment.

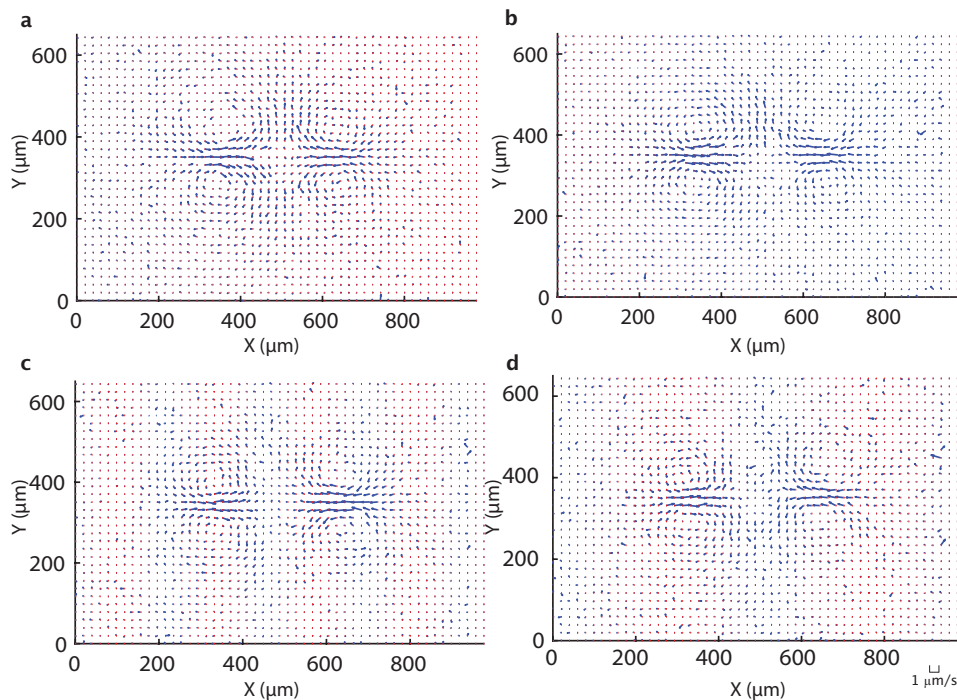


Figure 2.22: Velocity field averaged over 7.5 minute intervals in a single experiment. Time-windows are **a**,  $t = 0 - 7.5$  min **b**,  $t = 7.5 - 15$  min **c**,  $t = 15 - 22.5$  min **d**,  $t = 22.5 - 30$  min.

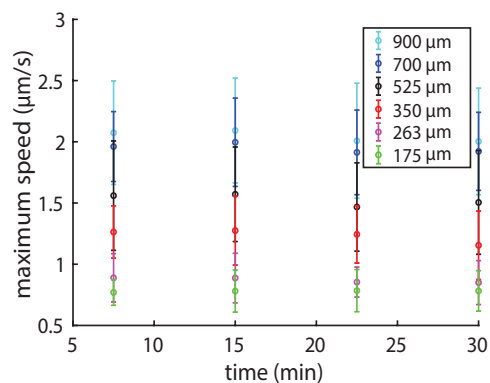


Figure 2.23: The average maximum speed for four different 7.5 minute time windows. The data points represent the average of nine experiments. The error bars are the associated standard deviation.

### 2.5.5 Generation of Streamline Plots

Streamlines are the spatial path traced out by fiducial points moving with the fluid flow. They can be numerically generated from a velocity vector field. To generate the streamlines shown in Fig. 2.15c, g, we use the streamplot function found in the Matplotlib Python library. First, the streamplot function maps a user-defined grid

onto the velocity vector field, which determines the density of the streamlines. Next, streamplot creates trajectories from a subset of velocity vectors by performing an interpolation from the current position  $x(t)$  of the streamline to the next position  $x(t + dt)$  based on the velocity  $v(x(t))$  by a 2nd-order Runge-Kutta algorithm. To prevent streamlines from crossing, a mask is defined around each interpolated trajectory, which excludes other trajectories from entering into the mask.

### 2.5.6 Correlation Length

The flow patterns that we observe have vortices. We can characterize the spatial extent of patterns like vortices by the velocity–velocity correlation coefficient  $C(R)$  [6, 39]:

$$C(R) = \frac{\langle V(R) \cdot V(0) \rangle}{\langle |V(0)|^2 \rangle} \quad (2.23)$$

where  $V$  is the fluid velocity vector,  $R$  is the distance between velocity vectors,  $\langle \rangle$  denotes ensemble average, and  $\|$  is the magnitude of the vector. The correlation length  $L_c$  is defined as the distance when  $C(L_c) = 0$ . This is the length scale where velocity vectors change to an orthogonal direction. By definition,  $C(0) = 1$ . The correlation coefficient as a function of  $R$  is calculated to determine  $L_c$  for each bar length (Fig. 2.24).

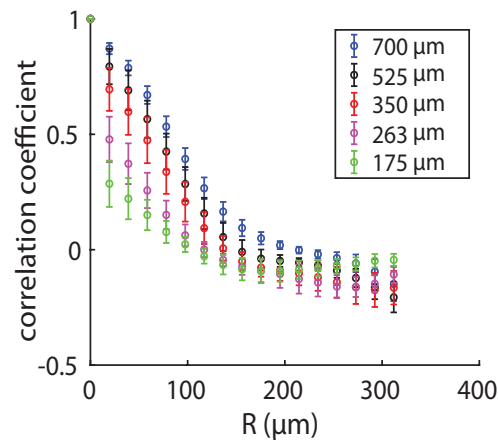


Figure 2.24: The correlation coefficient as a function of distance. Each marker shows that the mean over nine individual experiments and error bars are the associated standard deviation.

### 2.5.7 Theoretical Model of the Fluid Flow Field

We use solutions of the Stokes equation, the governing equation for fluid flow at low-Reynolds-number [40], to model our induced flow fields. One of the simplest

solutions of the equation is the Stokeslet, which describes the flow field induced by a point force [41]. Here, we attribute the flow-generating point forces to contracting microtubule bundles. Since the microtubules at the center of the activation bar appear to contract much more slowly than in other regions of the light pattern, we do not model Stokeslets in the central 120  $\mu\text{m}$  of the activation bar. We superimpose the solutions for two series of Stokeslets, one for each side of the bar. Each series of Stokeslets is composed of 7 point forces with identical magnitude ( $|\mathbf{f}| = 2 \text{ nN}$ ), separated by 20  $\mu\text{m}$  (Fig. 2.25) to model the 350  $\mu\text{m}$  activation bar case.

The velocity field  $\mathbf{u}(\mathbf{x})$  generated by a point force  $\mathbf{f}$  located at  $\mathbf{x}'$  in a 2D plane is given as

$$\mathbf{u}(\mathbf{x}) = \frac{1}{4\pi\eta} \left( -\mathbf{f} \log(r) + \frac{(\mathbf{f} \cdot (\mathbf{x} - \mathbf{x}'))(\mathbf{x} - \mathbf{x}')}{r^2} \right) \quad (2.24)$$

where  $\eta$  is the fluid viscosity and  $r$  is the absolute distance, defined as

$$r = |\mathbf{x} - \mathbf{x}'|. \quad (2.25)$$

We estimate  $\eta = 2 \times 10^{-3} \text{ Pa} \cdot \text{s}$  (Section 2.5.8).

Comparing Fig. 2.25 to Fig. 2.20, for the rectangular bar experiment, we see that our model recovers the general pattern of inflows and outflows in magnitude and direction. In both figures, the inflows along the X direction and the outflows along the Y direction are asymmetric in magnitude, with the inflows being greater than the outflows. However, in the experiments, there can be additional asymmetries not captured by the model. For example in Fig. 2.20, outflows in the downward direction (Y-axis,  $Y < 300 \mu\text{m}$ ) appear greater in magnitude than the outflows in the upward direction (Y-axis,  $Y > 300 \mu\text{m}$ ). This may be related to the microtubule buckling shown in Fig. 2.15b, which leads to asymmetry of the microtubule network density in the last panel of Fig. 2.15a. Further, we note that we do not observe vortices for our model parameters. It is possible that the presence of vortices may lead to additional effects not generated by the current model.

There are various candidate mechanisms for vortex generation - boundary conditions, zones of depleted microtubules, and non-Newtonian fluid properties, to list a few. Further investigation will be needed to determine which of these effects, if any, cause the observed vortices.

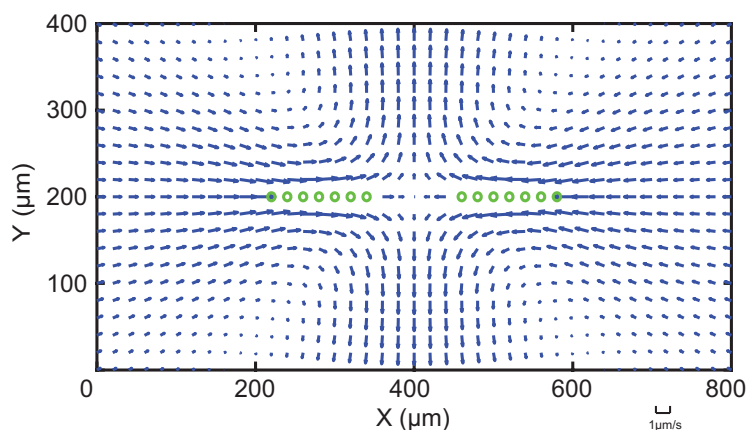


Figure 2.25: Flow field generated by 14 Stokeslets, indicated by green circles, to model the 350  $\mu\text{m}$  activation bar case. This theoretical model recovers the general pattern of inflows and outflows observed in the experiment (Fig. 4a), but not the vortices and asymmetries in flow magnitudes.

Due to the linear nature of low-Reynolds-number flow [42], we expect that the velocity field generated by a complex light pattern can be retrieved by superposition of simple patterns. To confirm this, we superimpose flow fields from single bars to mimic the flow field generated by “L”, “+” and “T”-shaped light patterns (Fig. 2.26). For the “+” case, the superimposed fields closely resemble the experimentally observed field (Fig. 2.26c). The “L” and “T”-shaped cases are roughly similar to the experimental results, but direction of the inflows do not match (Fig. 2.26b, d).

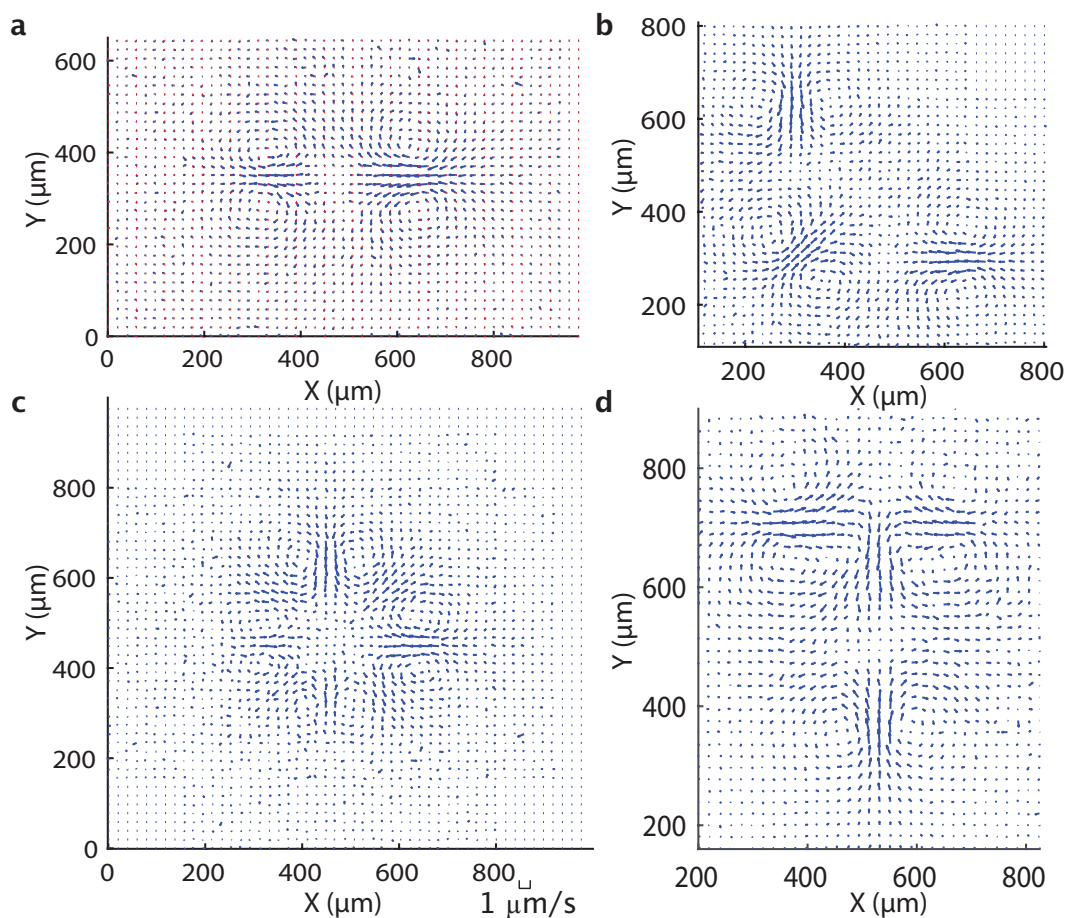


Figure 2.26: Demonstration of the linearity of the flow field. **a**, A time averaged flow field generated by a  $350\ \mu\text{m}$  rectangular bar. Flow fields generated by the rotation and superposition of the flow field in **(a)** to retrieve flow fields for **b**, “L” **c**, “+”, and **d**, “T”-shaped light patterns.

To model the “L” and “T” flow fields more accurately, we generate the flow field for a series of Stokeslets following the geometry of the microtubule structure, rather than the light pattern itself. Using this method, the modeled flow fields are a good approximation of the observed flow fields. The inflows and outflows match the experimentally observed positions and orientations (Fig. 2.27). This result implies that the observed flow patterns are set by the microtubule structure rather than the light pattern.

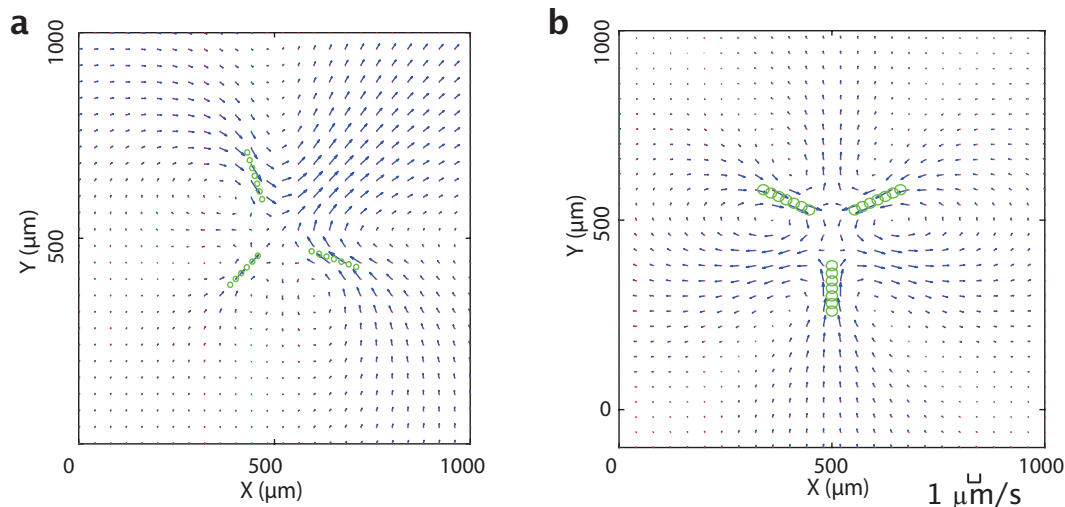


Figure 2.27: Theoretical simulation of fluid flows under complex light patterns using Stokeslets. The Stokeslets are positioned following the shape of the microtubule network observed in Fig. 4f. Green circles denote the Stokeslets. **a**, Flow field for “L”-shaped light pattern. **b**, Flow field for “T”-shaped light pattern.

## 2.5.8 Calculating Fluid Viscosity

To find the viscosity of the background buffer, we used a similar approach to finding the flow fields. We used PTV of fiducial tracer particles (Supplemental Information 2.5.2) in inactivated regions of the sample of the 175  $\mu\text{m}$  activation bar experiment. Assuming the buffer is Newtonian [43], the inert tracer particles diffuse freely due to thermal fluctuations. From the tracking results, we measure the mean-squared displacement  $\text{MSD}(t)$  of the particles:

$$\text{MSD}(t) = \langle (x(t) - x(0))^2 + (y(t) - y(0))^2 \rangle, \quad (2.26)$$

where  $x(t)$  and  $y(t)$  are the position of a given particle at time  $t$  and  $\langle \rangle$  denotes ensemble average. For this calculation, each frame is  $t = 4$  s apart. The  $\text{MSD}(t)$  of a freely diffused particle in 2D follows the Stokes-Einstein equation

$$\text{MSD}(t) = 4Dt = \frac{2k_B T}{3\pi\eta r} t, \quad (2.27)$$

where  $r = 0.5 \mu\text{m}$  is the radius of the particle. Then, the viscosity of the buffer solution is estimated as

$$\eta = \frac{8k_B T}{3\pi r \text{MSD}(t)}. \quad (2.28)$$

The same process is repeated through nine individual experiments and the average estimated viscosity  $\eta$  is  $2 \times 10^{-3} \text{ Pa} \cdot \text{s}$ .

## 2.6 Conclusion

In this work, we uncover active matter phenomena through the creation and manipulation of non-equilibrium structures and resultant fluid flows. Our ability to define boundaries of protein activity with light enables unprecedented control of an active matter system's organization (Supplemental Information 2.6.1). We find scaling rules of contractile networks, movement of non-equilibrium structures, and modulation of flow fields. This framework may be built upon to create active matter devices that control fluid flow. Future work will explore spatiotemporal limits of non-equilibrium structures, the interplay of mass flows and structural changes, and develop new theories of non-equilibrium mechanics and dynamics. Our approach of understanding through construction creates a path towards a generalizable theory of non-equilibrium systems, engineering with active matter, and understanding biological phenomena.

### 2.6.1 Comparison to Optically Controlled Bacteria

The polarity of the motors and microtubules makes them distinct from systems based on optically controlled bacteria [44, 45]. In our work, the localization of motor linkages causes microtubules to collectively reorganize into contracting networks. Due to the organization of microtubules and resulting dipolar stresses on the surrounding medium, we are able to create coherent flows. In contrast, localization of the activity of bacterial swimmers results in a change in the bacterial density, but lacks structural order and therefore does not generate coherent flows. However, bacterial densities can form arbitrary patterns that directly correspond to the optical projections analogous to photolithography. The resolution of the patterns we can create (Section 2.5.1) is generally lower than the reported  $\approx 2 \mu\text{m}$  resolution achievable with bacterial swimmers. Light in our system does not directly pattern microtubules, but rather defines an effective reaction volume where certain reorganizing motifs can occur.

## 2.7 Methods and Materials

### 2.7.1 Kinesin Chimera Construction and Purification

To introduce optical control, we implemented the light-induced hetero-dimer system of iLID and SspB-micro [14]. We constructed two chimeras of *D. melanogaster* kinesin K401: K401-iLID and K401-micro (Fig S1).



Figure 2.28: Kinesin motor coding regions.

To construct the K401-iLID plasmid (Addgene 122484), we PCR amplified the coding region of iLID from the plasmid pQE-80L iLID (gift from Brian Kuhlman, Addgene 60408) and used Gibson assembly to insert it after the C-terminus of K401 in the plasmid pBD-0016 (gift from Jeff Gelles, Addgene 15960). To construct the K401-micro plasmid (Addgene 122485), we PCR amplified the coding region of K401 from the plasmid pBD-0016 and used Gibson assembly to insert it in between the His-MBP and micro coding regions of plasmid pQE-80L MBP-SspB Micro (gift from Brian Kuhlman, Addgene 60410). As reported in [14], the MBP domain is needed to ensure that the micro domain remains fully functional during expression. Subsequent to expression, the MBP domain can be cleaved off by utilizing a TEV protease site.

For protein purification, we used the His tags that were provided by the base plasmids. For protein expression, we transformed the plasmids into BL21(DE3)pLysS cells. The cells were induced at OD 0.6 with 1 mM IPTG and grown for 16 hours at 18°C. The cells were pelleted and then resuspended in lysis buffer (50 mM sodium phosphate, 4 mM MgCl<sub>2</sub>, 250 mM NaCl, 25 mM imidazole, 0.05 mM MgATP, 5 mM BME, 1 mg/ml lysozyme and 1 tablet/50 mL of Complete Protease Inhibitor). After an hour, the lysate was passed through a 30 kPSI cell disruptor to lyse any remaining cells. The lysate was then clarified by an ultra-centrifuge spin at 30,000 g for 1 hour. The clarified lysate was incubated with Ni-NTA agarose resin (Qiagen 30210) for 1 hour. The lysate mixture was loaded into a chromatography column, washed three times with wash buffer (lysis buffer without lysozyme and protease inhibitor), and eluted with 500 mM imidazole. For the K401-micro elution, we added TEV protease at a 1:25 mass ratio to remove the MBP domain. Protein elutions were dialyzed overnight using a 30 kDa MWCO membrane to reduce trace imidazole and small protein fragments. Protein was concentrated with a centrifugal filter (EMD Millipore UFC8030) to 8-10 mg/ml. Protein concentrations were determined by absorption of 280 nm light with a UV spectrometer.

### 2.7.2 Microtubule Polymerization and Length Distribution

We polymerized tubulin with the non-hydrolyzable GTP analog GMP-CPP, using a protocol based on the one found on the Mitchison lab homepage [46]. A polymerization mixture consisting of M2B buffer (80 mM K-PIPES pH 6.8, 1 mM EGTA, 2 mM MgCl<sub>2</sub>), 75  $\mu$ M unlabeled tubulin (PurSolutions 032005), 5  $\mu$ M tubulin-AlexaFluor647 (PurSolutions 064705), 1 mM DTT, and 0.6 mM GMP-CPP (Jenna Biosciences NU-405S) was spun at  $\approx$  300,000 g for 5 minutes at 2°C to pellet aggregates. The supernatant was then incubated at 37°C for 1 hour to form GMP-CPP stabilized microtubules.

To measure the length distribution of microtubules, we imaged fluorescently labeled microtubules immobilized onto the cover glass surface of a flow cell. The cover glass was treated with a 0.01% solution of poly-L-lysine (Sigma P4707) to promote microtubule binding. The lengths of microtubules were determined by image segmentation. To reduce the effect of the non-uniformity in the illumination, we apply a Bradley adaptive threshold with a sensitivity of 0.001 and binarize the image. Binary objects touching the image border and smaller than 10 pixels in size were removed. To connect together any masks that were “broken” by the thresholding, a morphological closing operation was performed with a 3-pixel  $\times$  3-pixel neighborhood. Masks of microtubules are then converted into single pixel lines by applying a morphological thinning followed by a removal of pixel spurs. The length of a microtubule is determined by counting the number of pixels that make up each line and multiplying it by the interpixel distance. For the characteristic microtubule length, we report the mean of the measured lengths (Fig. 2.29). For comparison, we also fit an exponential distribution to the observed histogram. We note that a full distribution of microtubule lengths does not, in general, follow an exponential decay, however, the exponential has been shown to be appropriate for limited length spans [47].

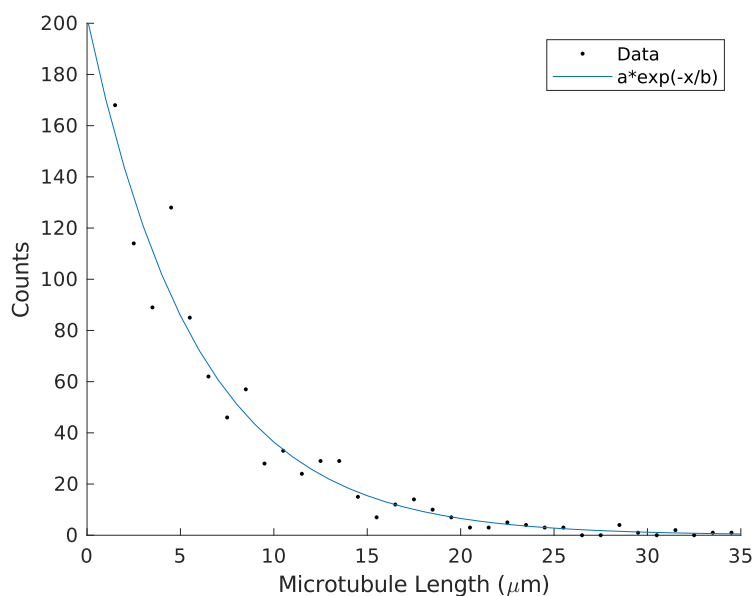


Figure 2.29: Length distribution of microtubules. The mean length given by the data histogram is  $7 \pm 0.2\mu\text{m}$ , where the  $\pm$  indicates the standard error of the mean. This mean length is similar to the  $\approx 6\mu\text{m}$  mean length given by a fit to an exponential distribution.

### 2.7.3 Sample Chambers for Aster and Flow Experiments

For the aster and flow experiments, microscope slides and cover glass are passivated against non-specific protein absorption with a hydrophilic acrylamide coating [48]. The glass is first cleaned in a multi-step alkaline etching procedure that removes organics and the surface layer of the glass. The slides and cover glass are immersed and sonicated for 30 minutes successively in 1% Hellmanex III (Helma Analytics) solution, followed by ethanol, and finished in 0.1 M KOH solution. After cleaning, the glass is immersed in a silanizing solution of 98.5% ethanol, 1% acetic acid, and 0.5% 3-(Trimethoxysilyl)propylmethacrylate (Sigma 440159) for 10-15 min. After rinsing, the slides are immersed overnight in a degassed 2 % acrylamide solution with 0.035% TEMED and 3 mM ammonium persulfate. Just before use, the glass is rinsed in distilled water and nitrogen dried. Parafilm M gaskets with pre-cut 3 mm wide channels are used to seal the cover glass and slide together, making a flow cell that is  $\approx 70\mu\text{m}$  in height. After the addition of the reaction mixture, a flow cell lane is sealed with a fast setting silicone polymer (Picodent Twinsil Speed).

#### **2.7.4 Reaction Mixture and Sample Preparation for Aster and Flow Experiments**

For the aster and flow experiments, K401-micro, K401-iLID, and microtubules were combined into a reaction mixture, leading to final concentrations of  $\approx 0.1 \mu\text{M}$  of each motor type and  $1.5\text{-}2.5 \mu\text{M}$  of tubulin. Concentrations refer to protein monomers for the K401-micro and K401-iLID constructs and the protein dimer for tubulin. To minimize unintended light activation, the sample was prepared under dark-room conditions, where the room light was filtered to block wavelengths below 580 nm (Kodak Wratten Filter No. 25). The base reaction mixture provided a buffer, an energy source (MgATP), a crowding agent (glycerol), a surface passivating polymer (pluronic F-127), oxygen scavenging components to reduce photobleaching (glucose oxidase, glucose, catalase, Trolox, DTT), and ATP-recycling reagents to prolong motor activity (pyruvate kinase/lactic dehydrogenase, phosphoenolpyruvic acid). The reaction mixture consisted of 59.2 mM K-PIPES pH 6.8, 4.7 mM  $\text{MgCl}_2$ , 3.2 mM potassium chloride, 2.6 mM potassium phosphate, 0.74 mM EGTA, 1.4 mM MgATP (Sigma A9187), 10% glycerol, 0.50 mg/mL pluronic F-127 (Sigma P2443), 0.22 mg/ml glucose oxidase (Sigma G2133), 3.2 mg/ml glucose, 0.038 mg/ml catalase (Sigma C40), 5.4 mM DTT, 2.0 mM Trolox (Sigma 238813), 0.026 units/ $\mu\text{l}$  pyruvate kinase/lactic dehydrogenase (Sigma P0294), and 26.6 mM phosphoenolpyruvic acid (Beantown Chemical 129745).

We note that the sample is sensitive to the ratio of motors and microtubules and the absolute motor concentration. When the motor concentration is below  $0.1 \mu\text{M}$  for K401-micro and K401-iLID, light patterns are able to create microtubule bundles or lattices of small asters, similar to the phases observed as functions of motor concentration described in [5]. If this motor concentration is above  $\approx 2 \mu\text{M}$ , however, the number of binding events between inactivated K401-micro and K401-iLID proteins is sufficient to cause the spontaneous microtubule bundling and aster formation.

#### **2.7.5 Sample Preparation for Gliding Assay**

For the gliding assay experiments, microscope slides and cover glass are coated with antibodies to specifically bind motor proteins. First, alkaline cleaned cover glass and ethanol scrubbed slides were prepared and  $5 \mu\text{L}$  flow chambers were prepared with double-sided tape. Motors were bound to the surface by successive incubations of the chamber with  $400 \mu\text{g/mL}$  penta-His antibody (Qiagen 34660) for 5 min,  $10 \text{ mg/ml}$  whole casein (Sigma C6554) for 5 min, and finally motor protein

(1mg/mL in M2B) for 5 min. Unbound motors were washed out with M2B buffer, then AlexaFluor 647 labeled GMP-CPP stabilized microtubules in M2B with 5 mM MgATP and 1mM DTT were flowed in.

### 2.7.6 Preparation of Tracer Particles

To measure the fluid velocity, we used 1  $\mu\text{m}$  polystyrene beads (Polysciences 07310-15) as tracer particles. To passivate the hydrophobic surface of the beads, we incubated them overnight in M2B buffer with 50 mg/ml of pluronic F-127. Just before an experiment, the pluronic coated beads are washed by pelleting and resuspending in M2B buffer with 0.5 mg/ml pluronic to match the pluronic concentration of the reaction mixture.

### 2.7.7 Microscope Instrumentation

We performed the experiments with an automated widefield epifluorescence microscope (Nikon TE2000). We custom modified the scope to provide two additional modes of imaging: epi-illuminated pattern projection and LED gated transmitted light. We imaged light patterns from a programmable DLP chip (EKB Technologies DLP LightCrafter™ E4500 MKII™ Fiber Couple) onto the sample through a user-modified epi-illumination attachment (Nikon T-FL). The DLP chip was illuminated by a fiber coupled 470 nm LED (ThorLabs M470L3). The epi-illumination attachment had two light-path entry ports, one for the projected pattern light path and the other for a standard widefield epi-fluorescence light path. The two light paths were overlapped with a dichroic mirror (Semrock BLP01-488R-25). The magnification of the epi-illuminating system was designed so that the imaging sensor of the camera (FliR BFLY-U3-23S6M-C) was fully illuminated when the entire DLP chip was on. Experiments were run with Micro-Manager [49], running custom scripts to controlled pattern projection and stage movement. For the transmitted light path, we replaced the standard white-light brightfield source (Nikon T-DH) with an electronically time-gated 660 nm LED (ThorLabs M660L4-C5). This was done to minimize light-induced dimerization during bright field imaging.

## References

1. Marchetti, M. C., Joanny, J. F., Ramaswamy, S., Liverpool, T. B., Prost, J., Rao, M. & Simha, R. A. Hydrodynamics of soft active matter. *Reviews of Modern Physics* **85**, 1143–1189. doi:10.1103/RevModPhys.85.1143 (2013).

2. Dumont, S. & Prakash, M. Emergent mechanics of biological structures. *Molecular Biology of the Cell* **25**, 3461–3465. ISSN: 1059-1524, 1939-4586. doi:10.1091/mbc.E14-03-0784 (2014).
3. Needleman, D. & Dogic, Z. Active matter at the interface between materials science and cell biology. *Nature Reviews Materials* **2**, 17048. ISSN: 2058-8437. doi:10.1038/natrevmats.2017.48 (2017).
4. Nédélec, F. J., Surrey, T., Maggs, A. C. & Leibler, S. Self-organization of microtubules and motors. *Nature* **389**, 305. ISSN: 1476-4687. doi:10.1038/38532 (1997).
5. Surrey, T., Nédélec, F., Leibler, S. & Karsenti, E. Physical Properties Determining Self-Organization of Motors and Microtubules. *Science* **292**, 1167–1171. ISSN: 0036-8075, 1095-9203. doi:10.1126/science.1059758 (2001).
6. Sanchez, T., Chen, D. T. N., DeCamp, S. J., Heymann, M. & Dogic, Z. Spontaneous motion in hierarchically assembled active matter. *Nature* **491**, 431. ISSN: 1476-4687. doi:10.1038/nature11591 (2012).
7. DeCamp, S. J., Redner, G. S., Baskaran, A., Hagan, M. F. & Dogic, Z. Orientational order of motile defects in active nematics. *Nature Materials* **14**, 1110. ISSN: 1476-4660. doi:10.1038/nmat4387 (2015).
8. Wu, K.-T., Hishamunda, J. B., Chen, D. T. N., DeCamp, S. J., Chang, Y.-W., Fernández-Nieves, A., Fraden, S. & Dogic, Z. Transition from turbulent to coherent flows in confined three-dimensional active fluids. *Science* **355**, eaal1979. ISSN: 0036-8075, 1095-9203 (2017).
9. Bricard, A., Caussin, J.-B., Desreumaux, N., Dauchot, O. & Bartolo, D. Emergence of macroscopic directed motion in populations of motile colloids. *Nature* **503**, 95–98. ISSN: 1476-4687. doi:10.1038/nature12673 (2013).
10. Nédélec, F., Surrey, T. & Maggs, A. C. Dynamic Concentration of Motors in Microtubule Arrays. *Physical Review Letters* **86**, 3192–3195. doi:10.1103/PhysRevLett.86.3192 (2001).
11. Lee, H. Y. & Kardar, M. Macroscopic equations for pattern formation in mixtures of microtubules and molecular motors. *Physical Review. E, Statistical, Nonlinear, and Soft Matter Physics* **64**, 056113. ISSN: 1539-3755. doi:10.1103/PhysRevE.64.056113 (2001).
12. Keber, F. C., Loiseau, E., Sanchez, T., DeCamp, S. J., Giomi, L., Bowick, M. J., Marchetti, M. C., Dogic, Z. & Bausch, A. R. Topology and dynamics of active nematic vesicles. *Science* **345**, 1135–1139. ISSN: 0036-8075, 1095-9203. doi:10.1126/science.1254784 (2014).
13. Aoyama, S., Shimoike, M. & Hiratsuka, Y. Self-organized optical device driven by motor proteins. *Proceedings of the National Academy of Sciences* **110**, 16408–16413. ISSN: 0027-8424, 1091-6490. doi:10.1073/pnas.1306281110 (2013).

14. Guntas, G., Hallett, R. A., Zimmerman, S. P., Williams, T., Yumerefendi, H., Bear, J. E. & Kuhlman, B. Engineering an improved light-induced dimer (iLID) for controlling the localization and activity of signaling proteins. *Proceedings of the National Academy of Sciences of the United States of America* **112**, 112–117. ISSN: 1091-6490. doi:10.1073/pnas.1417910112 (2015).
15. Schuppler, M., Keber, F. C., Kröger, M. & Bausch, A. R. Boundaries steer the contraction of active gels. *Nature Communications* **7**, 13120. ISSN: 2041-1723. doi:10.1038/ncomms13120 (2016).
16. Belmonte, J. M., Leptin, M. & Nédélec, F. A theory that predicts behaviors of disordered cytoskeletal networks. *Molecular Systems Biology* **13**, 941. doi:10.15252/msb.20177796. eprint: <https://onlinelibrary.wiley.com/doi/pdf/10.15252/msb.20177796> (2017).
17. Foster, P. J., Fürthauer, S., Shelley, M. J. & Needleman, D. J. Active contraction of microtubule networks. *eLife* **4**, e10837 (2015).
18. Good, M. C., Vahey, M. D., Skandarajah, A., Fletcher, D. A. & Heald, R. Cytoplasmic Volume Modulates Spindle Size During Embryogenesis. *Science* **342**, 856–860. ISSN: 0036-8075, 1095-9203. doi:10.1126/science.1243147 (2013).
19. Lenz, M., Thoresen, T., Gardel, M. L. & Dinner, A. R. Contractile Units in Disordered Actomyosin Bundles Arise from F-Actin Buckling. *Physical Review Letters* **108**, 238107. doi:10.1103/PhysRevLett.108.238107 (23 2012).
20. Tas, R. P., Chen, C.-Y., Katrukha, E. A., Vleugel, M., Kok, M., Dogterom, M., Akhmanova, A. & Kapitein, L. C. Guided by Light: Optical Control of Microtubule Gliding Assays. *Nano Letters* **0**. PMID: 30449112, null. doi:10.1021/acs.nanolett.8b03011 (2018).
21. Nakamura, H., Lee, A. A., Afshar, A. S., Watanabe, S., Rho, E., Razavi, S., Suarez, A., Lin, Y.-C., Tanigawa, M., Huang, B., *et al.* Intracellular production of hydrogels and synthetic RNA granules by multivalent molecular interactions. *Nature Materials* **17**, 79 (2018).
22. Johnson, H. E., Goyal, Y., Pannucci, N. L., Schüpbach, T., Shvartsman, S. Y. & Toettcher, J. E. The spatiotemporal limits of developmental ERK signaling. *Developmental Cell* **40**, 185–192 (2017).
23. Yumerefendi, H., Lerner, A. M., Zimmerman, S. P., Hahn, K., Bear, J. E., Strahl, B. D. & Kuhlman, B. Light-induced nuclear export reveals rapid dynamics of epigenetic modifications. *Nature Chemical Biology* **12**, 399 (2016).
24. Tirado, M. M. & de la Torre, J. G. Translational friction coefficients of rigid, symmetric top macromolecules. Application to circular cylinders. *The Journal of Chemical Physics* **71**, 2581–2587. doi:10.1063/1.438613 (1979).

25. Weiner, O. D., Marganski, W. A., Wu, L. F., Altschuler, S. J. & Kirschner, M. W. An Actin-Based Wave Generator Organizes Cell Motility. *PLOS Biology* **5**, 1–11. doi:10.1371/journal.pbio.0050221 (2007).
26. Gardel, M. L., Schneider, I. C., Aratyn-Schaus, Y. & Waterman, C. M. Mechanical Integration of Actin and Adhesion Dynamics in Cell Migration. *Annual Review of Cell and Developmental Biology* **26**, 315–333 (2010).
27. Svoboda, K. & Block, S. M. Biological Applications of Optical Forces. *Annual Review of Biophysics and Biomolecular Structure* **23**, 247–285 (1994).
28. Mahamdeh, M., Perez Campos, C. & Schäffer, E. Under-Filling Trapping Objectives Optimizes the use of Available Laser Power in Optical Tweezers. *Optics express* **19**, 11759–68. doi:10.1364/OE.19.011759 (2011).
29. Theurkauf, W. E. Premature microtubule-dependent cytoplasmic streaming in cappuccino and spire mutant oocytes. *Science* **265**, 2093–2096 (1994).
30. Ganguly, S., Williams, L. S., Palacios, I. M. & Goldstein, R. E. Cytoplasmic streaming in *Drosophila* oocytes varies with kinesin activity and correlates with the microtubule cytoskeleton architecture. *Proceedings of the National Academy of Sciences* **109**, 15109–15114 (2012).
31. Goldstein, R. E., Tuval, I. & van de Meent, J.-W. Microfluidics of cytoplasmic streaming and its implications for intracellular transport. *Proceedings of the National Academy of Sciences* **105**, 3663–3667 (2008).
32. Drescher, K., Dunkel, J., Cisneros, L. H., Ganguly, S. & Goldstein, R. E. Fluid dynamics and noise in bacterial cell–cell and cell–surface scattering. *Proceedings of the National Academy of Sciences* **108**, 10940–10945 (2011).
33. Drescher, K., Goldstein, R. E., Michel, N., Polin, M. & Tuval, I. Direct Measurement of the Flow Field around Swimming Microorganisms. *Physical Review Letters* **105**, 168101. doi:10.1103/PhysRevLett.105.168101 (2010).
34. He, B., Doubrovinski, K., Polyakov, O. & Wieschaus, E. Apical constriction drives tissue-scale hydrodynamic flow to mediate cell elongation. *Nature* **508**, 392 (2014).
35. Shinar, T., Mana, M., Piano, F. & Shelley, M. J. A model of cytoplasmically driven microtubule-based motion in the single-celled *Caenorhabditis elegans* embryo. *Proceedings of the National Academy of Sciences* **108**, 10508–10513. ISSN: 0027-8424. doi:10.1073/pnas.1017369108. eprint: <https://www.pnas.org/content/108/26/10508.full.pdf> (2011).
36. Mittasch, M., Gross, P., Nestler, M., Fritsch, A. W., Iserman, C., Kar, M., Munder, M., Voigt, A., Alberti, S., Grill, S. W. & Kreysing, M. Non-invasive perturbations of intracellular flow reveal physical principles of cell organization. *Nature Cell Biology* **20**, 344–351. ISSN: 1476-4679. doi:10.1038/s41556-017-0032-9 (2018).

37. Maas, H., Gruen, A. & Papantoniou, D. Particle tracking velocimetry in three-dimensional flows. *Experiments in Fluids* **15**, 133–146 (1993).
38. Schmidt, T., Schütz, G., Baumgartner, W., Gruber, H. & Schindler, H. Imaging of single molecule diffusion. *Proceedings of the National Academy of Sciences* **93**, 2926–2929 (1996).
39. Dunkel, J., Heidenreich, S., Drescher, K., Wensink, H. H., Bär, M. & Goldstein, R. E. Fluid dynamics of bacterial turbulence. *Physical Review Letters* **110**, 228102 (2013).
40. Happel, J. & Brenner, H. *Low Reynolds number hydrodynamics: With special applications to particulate media* (Springer Science & Business Media, 2012).
41. Chwang, A. T. & Wu, T. Y.-T. Hydromechanics of low-Reynolds-number flow. Part 2. Singularity method for Stokes flows. *Journal of Fluid Mechanics* **67**, 787–815 (1975).
42. Kim, S. & Karrila, S. J. *Microhydrodynamics: Principles and selected applications* (Courier Corporation, 2013).
43. Panton, R. L. *Incompressible flow* (John Wiley & Sons, 2006).
44. Frangipane, G., Dell’Arciprete, D., Petracchini, S., Maggi, C., Saglimbeni, F., Bianchi, S., Vizsnyiczai, G., Bernardini, M. L. & Di Leonardo, R. Dynamic density shaping of photokinetic *E. coli*. *eLife* **7** (eds Goldstein, R. E. & Barkai, N.) e36608. ISSN: 2050-084X. doi:10.7554/eLife.36608 (2018).
45. Arlt, J., Martinez, V. A., Dawson, A., Pilizota, T. & Poon, W. C. K. Painting with light-powered bacteria. *Nature Communications* **9**, 768. ISSN: 2041-1723. doi:10.1038/s41467-018-03161-8 (2018).
46. Georgoulia, N. *Tubulin Polymerization with GTP/GMPCPP/Taxol* [https://mitchison.hms.harvard.edu/files/mitchisonlab/files/tubulin\\_polymerization\\_with\\_gtp.pdf](https://mitchison.hms.harvard.edu/files/mitchisonlab/files/tubulin_polymerization_with_gtp.pdf).
47. Gardner, M. K., Zanic, M. & Howard, J. Microtubule catastrophe and rescue. *Current Opinion in Cell Biology* **25**, 14–22. doi:10.1016/j.ceb.2012.09.006 (2013).
48. Lau, A. W. C., Prasad, A. & Dogic, Z. Condensation of isolated semi-flexible filaments driven by depletion interactions. *EPL (Europhysics Letters)* **87**, 48006 (2009).
49. Edelstein, A., Amodaj, N., Hoover, K., Vale, R. & Stuurman, N. Computer Control of Microscopes Using  $\mu$ Manager. *Current Protocols in Molecular Biology* **92**, 14.20.1–14.20.17 (2010).

*Chapter 3*

## DISCUSSION OF THE SPEED AMPLIFICATION EFFECT

The purpose of this chapter is to expand on the speed amplification effect observed in Chapter 2, which is shown in Fig. 2.1, Fig. 2.9f, and Fig. 2.15d. The speed amplification effect is the finding that microtubule contraction speeds increase as a function of the excitation boundary size. This result has not been previously observed in this type of system and may not be initially intuitive.

To begin, it is worth comparing this result to what has been observed in the leashed or gliding assay system. In the gliding assay, motor proteins are bound to a surface and push microtubules, causing the filaments to glide. Gliding experiments show that microtubules move along the surface at the average motor step speed [1]. In addition, no matter how many motor proteins are loaded onto the surface, the gliding speed of the microtubule remains the same. The finding that microtubules glide at the average motor speed is in stark contrast to what is observed in the unleashed system. The average speed of the light activated motors measured via gliding assay is  $\approx 300$  nm/s (Fig. 2.3.4). However, the fastest speed observed during aster merging is approximately an order of magnitude faster than the average motor speed (Fig. 2.9f).

The exact mechanism of the speed amplification effect has not been identified experimentally. However, a generic model predicts linear scaling of contraction speed as a function of size for 1D, 2D, and 3D networks [2]. Here I offer a simple model that may explain the speed amplification effect.

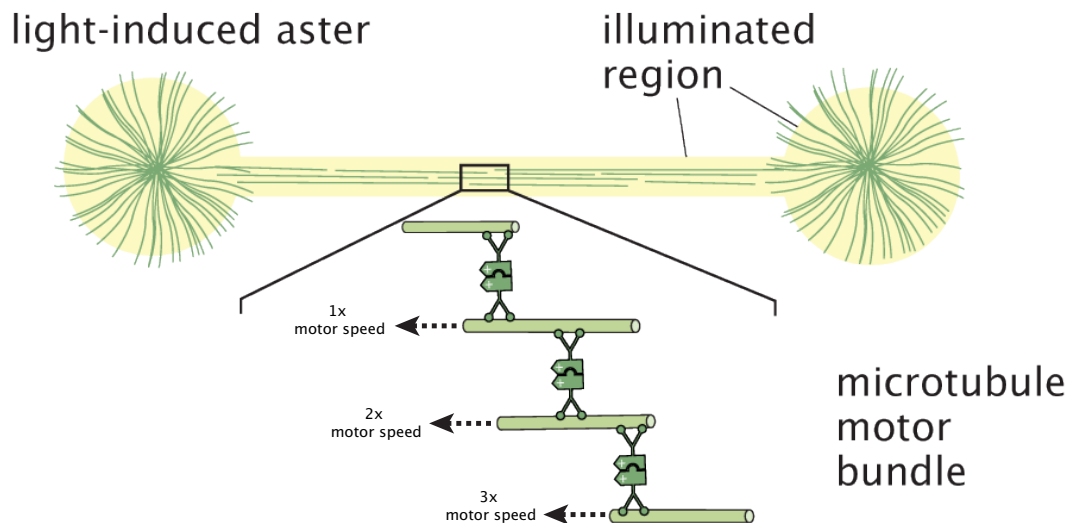


Figure 3.1: An illustration depicting a potential mechanism of the speed amplification effect in 1D.

For simplicity I will focus on a semi-1D system. The assumptions of this model are as follows:

1. Motor proteins dwell on the microtubule once they reach the plus end.
2. Anti-parallel microtubules can effectively be ignored.
3. Steric interactions between microtubules and motors are negligible.
4. The mechanical load experienced by an individual motor is low relative to its stall force.

As discussed in Chapter 1.2.2, the phenomenon of microtubules contracting together during aster formation appears to require that motors stay on the filaments when reaching the plus end. For this reason, I make assumption 1. The second assumption comes as a consequence of the first assumption. The tension generated by parallel bundles being pulled by plus-end dwelling motors will dominate the extensile forces from antiparallel filaments [3]. Assumption 3 is based on the observation that, during the initial contraction phase, the bundle of filaments that form continue to increase in density without visible evidence of buckling events. The fourth assumption comes from a calculation of the drag coefficient of a microtubule, which I approximate from the equation  $\gamma_{\parallel} = \frac{2\pi\eta L}{\ln(L/2r) - 0.20} = 0.02 \mu\text{m} \cdot \text{s} \cdot \text{Pa}$ , for  $L = 10 \mu\text{m}$ ,  $r = 12.5 \text{ nm}$  and  $\eta = 2 \times 10^{-3} \text{ Pa} \cdot \text{s}$  (see Chapter 2.2.11 for details). Based on this value,

a microtubule would have to be moving at approximately 230  $\mu\text{m/s}$  to reach a stall force of 5 pN. However, the fastest speed measured is on the order of two orders of magnitude slower than the calculated stall speed.

In the above illustration (Fig. 3.1) two asters are being pulled together through a bundle of contracting microtubule filaments. In this bundle I set a reference microtubule, which is at the top of the magnified region. A microtubule is connected to the reference filament via a motor pair. Due to the movement of the motors, the plus end of the connected microtubule will be pulled towards the plus end of the reference microtubule at 1x the motor speed. The addition of another microtubule motor pair to the microtubule that is already being pulled along the reference filament will move at 2x the motor speed. From here a pattern emerges. For each additional microtubule-motor pair, there is an additional 1x motor speed movement that contributes to the contractile motion. The end result is that filaments additively slide along each other as the plus ends are brought together. The movement described in this model is very similar to what is observed in colonies of *Bacillaria paxillifer*, where the rod-like unicellular organisms slide along each other [4].

Putting this model in mathematical terms,

$$[\text{Aster Speed}] \propto [\text{Motor Speed}] \frac{[\text{Size of Active Region}]}{\langle \text{Bundle Length} \rangle}. \quad (3.1)$$

Here  $\langle \text{Bundle Length} \rangle$  is the average distance between microtubule plus ends, and the size of the active region will be equal to the initial distance between asters. The stacking of motor-microtubule pairs should depend linearly on the motor speed and the size of the activation region, based on what has been described above. The intuition for the inverse dependence on the filament length is as follows. If the system is spanned by two microtubules that are half the length of the active region, then the contraction speed will be 1x the motor speed. If those microtubules are halved, the merger speed will similarly increase by a factor of two. The experiments in Chapter 2 shows the linear dependence of contraction speed on the size of the active region. Further experiments involving motors of different speeds and filaments of varying lengths would verify the validity of this model.

Expanding this model to 2D and 3D introduces the additional element of microtubule orientation. In the semi-1D model I presented, filaments are already aligned to be either parallel or antiparallel. However, for 2D and 3D systems, the system begins with a population of randomly oriented microtubules. This raises the question:

is microtubule alignment a necessary component of the speed amplification effect in this system? If so, how is filament alignment achieved? If alignment is not necessary, then the semi-1D model I present here needs to be modified or discarded all together. From the experimental data I have presented, there is no direct evidence that filaments are aligned in this manner during contraction. At present, the Phillips and Thomson labs are independently working on alternative and more detailed models and experiments to address these questions.

I offer my own speculation here. We know from experiment that a completely disordered field of microtubules forms bundles of contractile filaments that eventually organize into an aster. Therefore, microtubules must be reoriented at some point in this process. If one considers a pair of overlapping microtubules that are misaligned, the torques imparted by the motor linkages will bring filaments to more closely align with each other (see Fig. 4 in [5] for an illustration). Furthermore, there are likely multiple motor pairs walking across a single filament at any given time. The presence of additional motor bonds will further reinforce microtubule alignment. The picture becomes more complicated as more microtubules are introduced, however, I speculate that the torques that are seen in the two-filament scenario will cause larger numbers of microtubules to locally align into bundles. From this perspective, I suggest that the initial differences in microtubule alignment will only change the effective bundle length of the proposed model above. Testing this idea, however, may be difficult to achieve experimentally.

## References

1. Hancock, W. O. & Howard, J. Processivity of the Motor Protein Kinesin Requires Two Heads. *Journal of Cell Biology* **140**, 1395–1405. doi:10.1083/jcb.140.6.1395 (1998).
2. Belmonte, J. M., Leptin, M. & Nédélec, F. A theory that predicts behaviors of disordered cytoskeletal networks. *Molecular Systems Biology* **13**, 941. doi:10.15252/msb.20177796. eprint: <https://onlinelibrary.wiley.com/doi/pdf/10.15252/msb.20177796> (2017).
3. Kruse, K. & Jülicher, F. Actively Contracting Bundles of Polar Filaments. *Physical Review Letters* **85**, 1778–1781. doi:10.1103/physrevlett.85.1778 (2000).
4. Yamaoka, N., Suetomo, Y., Yoshihisa, T. & Sonobe, S. Motion analysis and ultrastructural study of a colonial diatom, *Bacillaria paxillifer*. *Microscopy* **65**, 211–221. doi:10.1093/jmicro/dfv375 (2016).

5. Nédélec, F. & Surrey, T. Dynamics of microtubule aster formation by motor complexes. *Comptes Rendus de l'Académie des Sciences - Series IV - Physics-Astrophysics* **2**, 841–847. doi:10.1016/s1296-2147(01)01227-6 (2001).

*Chapter 4*

## CONCLUSION

This thesis shows that spatial and temporal patterning of molecular interactions can lead to new aspects of active self-organization. The asters that are formed through patterned activity are shown to have their own mesoscopic properties in how they move and interact with each other. The behaviors of mesoscopic force fields, in the form of fluid flows, are also shown to depend on the geometry of the patterned activity and adapt to dynamic boundary conditions. Consequently, the mesoscopic behavior of the self-organizing system can be guided by varying the interactions between active molecules in space and time.

Based on these results, one might consider how spatial and temporal patterning can guide self-organization in other unleashed motor-filament systems (Fig. 1.1h-p). In the active gel or active nematic where a depletion force pushes filaments together, the flows observed in bulk solution have been spontaneous and random. Do cylindrical or toroidal patterns of activity generate flow patterns in the active gel similar to [1]? How do defects in the active nematic move in response to localized motor forces? How do the viscosity of the nematic and gel change as motor-filament interactions are varied in space and time? In order to address these questions, it will be necessary to derive theories that incorporate spatial and temporal variation in motor clustering. With these models, it will also be possible to explore more complex aspects of active self-organization. For example, what mesoscopic behaviors can one achieve in an unleashed system if motor-filament activity is determined by patterned signals generated within the sample instead of being externally guided?

The development of a self-organizing system that can respond to local/internal signals is a step towards the construction of a programmable and autonomous active material. A key challenge to building autonomy is finding a way to integrate information processing with self-organization behaviors. One clear route is to use the tools of molecular computation, where chemical reaction networks are constructed to perform logical operations [2]. As a simple first step, one might use an oscillating chemical signal to regulate the flows in an active gel, for example. More complex chemical signaling networks could then be made that locally determine the magnitude and direction of the flow field. Linking flow patterns to internal states

of the system could be of use for dynamically routing material on the mesoscopic length scale. However, even if we could perfectly implement arbitrarily complex logical circuits, the capabilities of any autonomous system will be limited by the types of self-organizing structures we can achieve.

The formation of more complex structures and force fields than asters and contractile bundles will require additional interaction rules between molecules. The self-organization of intricate structures in living matter, such as the flagella, require various scaffolding proteins [3]. It is likely that the our ability to form similar structures will require the development of scaffolds that impose geometric constraints on molecular interactions. In addition, one notable aspect that is missing from engineered active matter systems is control over filament polymerization. Polymerization motors are responsible for self-propulsion and cargo segregation in cells [4]. Purified tubulin monomers are unstable in solution, which is why majority of works use some form of stabilized microtubules. Therefore, the first step towards controlling microtubule polymerization will likely require finding a means to increase tubulin stability. Alternatively, there are biopolymers that are more stable, such as actin. However, the greatest challenge will be finding a mechanism that makes it possible to dynamically tune the rate of polymerization and depolymerization. Filament dynamics are controlled in cells by a multitude of signaling and binding proteins [5, 6]. The achievement of spatiotemporal control over polymerization will likely require protein engineering and/or the use of tunable inhibitors. Since the genetic sequences for actin and tubulin are evolutionarily conserved [7, 8], it may be difficult to find ways to modify either monomer without interfering with their primary functions. A more feasible approach might instead involve engineering capping, nucleating, and/or branching proteins [9–11] that are more amenable to modification.

Considering the challenges in working with proteins, ranging from stability issues to trouble with de novo design, it is reasonable to consider purely artificial alternatives. The most successful artificial molecular motors have been constructed out of DNA. These motors, which consist of multi-stranded DNA, traverse across a DNA track through a series of strand displacement reactions [12]. However, the fastest DNA walker moves at 300 nm/min, which is two orders of magnitude slower than protein motors. Alternatively, synthetic polymers have been made that undergo dynamic instability [13], however their reaction rates are on the order of hours as opposed to the seconds it takes for a microtubule to polymerize/depolymerize. In addition,

there are no motors that are currently able to interact with these filaments. Overall, there need to be substantial increases in the reaction rates of artificial motors and filaments in order to create an entirely synthetic self-organizing system.

Active self-organizing systems sit at the boundary of life. It is not difficult to imagine that someone will eventually construct a self-organizing system that is capable of self-propulsion and self-replication. Consequently, the principles of active self-organization should be applicable for both modeling the physics of living matter and for engineering cell-like machines.

The behavior of the cell's cytoskeleton will eventually be describable through the framework of self-organization. We may start to understand the long lists of cytoskeletal binding proteins [14, 15], not as an abstract network [16], but in terms of the molecular interaction rules they impose. The interaction rules between active molecules may be used to construct a physical model of the cytoskeleton that captures its self-organization dynamics. A physical model of the cytoskeleton will be able to provide insights into cytoskeletal malfunctions, which occur during cancer metastasis [17] and certain neurodegenerative diseases [18]. For example, metastatic cancer cells generate distinct protrusions known as invadopodia, which allow the cells to move through extracellular matrix and into other tissues. A physical model of the cytoskeleton could be used to predict ways that invadopodia formation can be prevented, which would reduce the likelihood of cancer metastasis. In the case of therapeutics, principles of self-organization might eventually be extended to build cell-like machines that can monitor a person's health and provide immediate treatment. For example, a modified cell or encapsulated artificial system might be engineered to patrol the body for viruses that normally attack or evade the immune system. Since living matter is the source of inspiration for finding principles of active self-organization, the idea of using these principles to understand, effect, and mimic cells does not require such a great leap of imagination. How might these principles be applied beyond biology?

More broadly, the principles of active self-organization may be used to create structures and phenomena that are not found in nature. For example, a system of self-propelled rods can exhibit the superfluid-like property of having a zero or negative viscosity [19]. Systems of rotating molecular gears powered by rotary motors, smart tracks that change behavior based on the history of what motors or cargo have moved across them, or a system of molecular motors that are coupled to

a magnetic field, have the potential to organize into complex structures that are not seen in biology. A combination of these molecular features might be used to create an active system that can transduce chemical energy into an electrical potential for powering an electronic device, for example. The creation of these active molecular systems will certainly require some ingenuity. The field of active matter is still in its early stages, and the possibilities for what artificial self-organizing systems can achieve is vast and ripe for exploration.

## References

1. Wu, K.-T., Hishamunda, J. B., Chen, D. T. N., DeCamp, S. J., Chang, Y.-W., Fernández-Nieves, A., Fraden, S. & Dogic, Z. Transition from turbulent to coherent flows in confined three-dimensional active fluids. *Science* **355**, eaal1979. ISSN: 0036-8075, 1095-9203 (2017).
2. Benenson, Y. Biomolecular computing systems: principles, progress and potential. *Nature Reviews Genetics* **13**, 455–468 (2012).
3. Berg, H. C. The rotary motor of bacterial flagella. *Annual Review of Biochemistry* **72** (2003).
4. Theriot, J. A. The Polymerization Motor. *Traffic* **1**, 19–28 (2000).
5. Lee, S. H. & Dominguez, R. Regulation of actin cytoskeleton dynamics in cells. *Molecules and Cells* **29**, 311–325 (2010).
6. Desai, A. & Mitchison, T. J. Microtubule polymerization dynamics. *Annual review of cell and developmental biology* **13**, 83–117 (1997).
7. Gunning, P. W., Ghoshdastider, U., Whitaker, S., Popp, D. & Robinson, R. C. The evolution of compositionally and functionally distinct actin filaments. *Journal of Cell Science* **128**, 2009–2019 (2015).
8. Ludueña, R. F. in *International Review of Cell and Molecular Biology* 41–185 (Elsevier, 2013).
9. Thawani, A., Kadzik, R. S. & Petry, S. XMAP215 is a microtubule nucleation factor that functions synergistically with the  $\gamma$ -tubulin ring complex. *Nature cell biology* **20**, 575–585 (2018).
10. Basnet, N., Nedožralova, H., Crevenna, A. H., Bodakuntla, S., Schlichthaerle, T., Taschner, M., Cardone, G., Janke, C., Jungmann, R., Magiera, M. M., *et al.* Direct induction of microtubule branching by microtubule nucleation factor SSNA1. *Nature Cell Biology* **20**, 1172–1180 (2018).
11. Galland, R., Leduc, P., Guérin, C., Peyrade, D., Blanchoin, L. & Théry, M. Fabrication of three-dimensional electrical connections by means of directed actin self-organization. *Nature Materials* **12**, 416–421 (2013).

12. Li, J., Johnson-Buck, A., Yang, Y. R., Shih, W. M., Yan, H. & Walter, N. G. Exploring the speed limit of toehold exchange with a cartwheeling DNA acrobat. *Nature Nanotechnology* **13**, 723–729 (2018).
13. Boekhoven, J., Hendriksen, W. E., Koper, G. J., Eelkema, R. & van Esch, J. H. Transient assembly of active materials fueled by a chemical reaction. *Science* **349**, 1075–1079 (2015).
14. Dos Remedios, C. G., Chhabra, D., Kekic, M., Dedova, I. V., Tsubakihara, M., Berry, D. A. & Nosworthy, N. J. Actin Binding Proteins: Regulation of Cytoskeletal Microfilaments. *Physiological Reviews* **83**, 433–473. ISSN: 0031-9333. doi:10.1152/physrev.00026.2002 (2003).
15. Goodson, H. V. & Jonasson, E. M. Microtubules and Microtubule-Associated Proteins. *Cold Spring Harbor Perspectives in Biology* **10**, a022608. ISSN: , 1943-0264. doi:10.1101/cshperspect.a022608 (2018).
16. Lazebnik, Y. Can a biologist fix a radio?—Or, what I learned while studying apoptosis. *Cancer Cell* **2**, 179–182 (2002).
17. Eddy, R. J., Weidmann, M. D., Sharma, V. P. & Condeelis, J. S. Tumor cell invadopodia: invasive protrusions that orchestrate metastasis. *Trends in cell biology* **27**, 595–607 (2017).
18. Cairns, N. J., Lee, V. M.-Y. & Trojanowski, J. Q. The cytoskeleton in neurodegenerative diseases. *The Journal of Pathology: A Journal of the Pathological Society of Great Britain and Ireland* **204**, 438–449 (2004).
19. Gao, T., Blackwell, R., Glaser, M. A., Betterton, M. & Shelley, M. J. Multiscale modeling and simulation of microtubule–motor-protein assemblies. *Physical Review E* **92**, 062709 (2015).